Climate Dynamics
https://doi.org/10.1007/s00382-024-07182-6

ORIGINAL ARTICLE

The diurnal cycle from observations and ERA5 in precipitation, clouds, boundary layer height, buoyancy, and surface fluxes

Aiguo Dai[1]

Received: 27 September 2023 / Accepted: 29 February 2024

Abstract

Diurnal variations in precipitation, clouds and other related fields are of interest for many applications. Here I analyze surface and satellite observations and ERA5 data to quantify these variations and evaluate ERA5's performance. Results show that ERA5 captures the observed seasonal climatology of precipitation and cloud amount remarkably well. Surface observations show that warm-season precipitation exhibits a robust diurnal cycle with an amplitude of ~ 20 to 50% of the daily mean and a peak around 14–18 local solar time (LST) over most land areas and 04–08 LST over most oceans. ERA5 approximately reproduces these features with a slightly earlier peak (by ~ 2 h) over both land and ocean and a stronger amplitude over land, mainly due to biases in its convective precipitation. The IMERG satellite product captures mainly the diurnal cycle of convective precipitation with a peak around 16–20 LST during the warm season. ERA5 oceanic precipitation shows robust diurnal variations that are comparable to observations despite its dampened marine surface diurnal cycle due to its use of daily-mean SST. This suggests a free-tropospheric control of oceanic precipitation diurnal cycle. Surface and satellite observations show more clouds (mainly from low clouds) during daytime (nighttime) over land (ocean). ERA5 total cloud diurnal anomalies are more comparable to surface observations than to ISCCP satellite product. Cloud base height shows a minimum in early afternoon and a maximum around midnight with a diurnal amplitude of ~ 150 m over warm-season land in surface observations; ERA5 approximately captures this diurnal cycle with a slightly stronger amplitude and earlier phase. Land planetary boundary layer height (PBLH) in ERA5 is around 250 m at night but increases after sunrise to a peak around 14–15 LST of about 1500–1900 m in the warm season and ~ 650 to 1100 m in the cold season, with largest diurnal amplitudes over summer drylands. ERA5 marine PBLH is higher in the cold season (~ 1000 m) than in the warm season (~ 530 m) in the extratropics, suggesting a dominant role by low-level wind-induced mixing. ERA5 CAPE shows out-of-phase diurnal variations over land and ocean, with near-noontime peak (minimum) and an early morning minimum (peak) over land (ocean). ERA5 CIN's diurnal cycle is approximately out of phase with CAPE. ERA5 captures well the diurnal cycles and their land–ocean and seasonal differences in surface net shortwave and longwave (LWnet) radiation seen in CERES satellite product, with a near-noontime peak in land LWnet. A near-noontime peak is also seen in ERA surface sensible and latent heat fluxes over land, while oceanic PBLH, LWnet and heat fluxes show little diurnal variation in ERA5, which may be partly due to its use of daily-mean SST.

Keywords Diurnal cycle · ERA5 · Precipitation · Clouds · Boundary layer · Surface fluxes

1 Introduction

Solar heating near the surface and in the atmosphere generates pronounced diurnal variations not only in air temperature, pressure, and winds (Dai 2023), but also in many other surface and atmospheric fields, such as precipitation, cloud cover, atmospheric instability and convection, planetary boundary layer height (PBLH), and surface energy and water fluxes. In particular, the precipitation diurnal cycle and the associated diurnal variations in clouds and

✉ Aiguo Dai
adai@albany.edu

[1] Department of Atmospheric and Environmental Sciences, University at Albany, State University of New York, Albany, NY 12222, USA

convection have been studied by a large number of papers (e.g., Ramage 1952; Kraus 1963; Wallace 1975; Oki and Musiake 1994; Dai et al. 1999; Dai 2001a; Ohsawa et al. 2001; Yang and Slingo 2001; Mapes et al. 2003; Nesbitt and Zipser 2003; Mori et al. 2004; Serra and McPhaden 2004; Yang and Smith 2006; Dai et al. 2007; Yu et al. 2007; Carbone and Tuttle 2008; Li et al. 2008; Zhou et al. 2008; Wang et al. 2011; Yuan et al. 2010, 2012; Yu and Li 2016; Yokoi et al. 2017; Du and Rotunno 2018; Sungmin and Kirstetter 2018; Wu et al. 2018; Tan et al. 2019; Zheng et al. 2019; Zhao et al. 2022, 2023a; Hayden et al. 2023). Because of its robust signal, short time scale, and linkage to convection and other processes, precipitation diurnal cycle has also been used as a testbed to evaluate cumulus and other parameterizations in climate and weather models (e.g., Randall et al. 1991; Dai et al. 1999; Lin et al. 2000; Dai and Trenberth 2004; Liang et al. 2004; Dai 2006; Lee et al. 2007a, b, 2008; Takayabu and Kimoto 2008; Ploshay and Lau 2010; Stratton and Stirling 2012; Wang et al. 2015, 2020; Covey et al. 2016; Mooney et al. 2017; Song and Zhang 2017, 2018; Wang and Hsu 2019; Xie et al. 2019; Cui et al. 2021; Lee and Wang 2021; Tang et al. 2021; Wei and Pu 2022; Chen et al. 2023a; Tao et al. 2023). Many studies also examined diurnal variations in cloudiness and convection (Gray and Jacobson 1977; Hendon and Woodberry 1993; Cairns 1995; Hahn et al. 1995; Rozendaal et al. 1995; Bergman and Salby 1996; Kondragunta and Gruber1996; Chen and Houze 1997; Sui et al. 1997; Soden 2000; Wylie and Woolf 2002; Tian et al. 2004; Stubenrauch et al. 2006; Ruppert and Johnson 2016; Noel et al. 2018; Chepfer et al. 2019; Chen et al. 2022, Cao et al. 2022; Zhao et al. 2023b), atmospheric instability (Dai et al. 1999; Bellenger et al. 2010; Ratnam et al. 2013; Tang et al. 2016), PBLH (Liu and Liang 2010; Seidel et al. 2012; Gu et al. 2020; Zhang et al. 2020; Guo et al. 2021), and surface fluxes (Zhang and Klein 2010; Clayson and Edson 2019; Yan et al. 2021; Zhu et al. 2023), although relatively few studies examined these diurnal variations on a global scale, which is needed for revealing any migrating wave patterns (Dai 2023).

Hourly to 3-hourly observations from rain-gauges, weather reports, weather radars and satellites have all been used to quantify precipitation diurnal cycle. During the warm season, precipitation and moist convection tend to occur more frequently in late afternoon over most land areas as daytime solar heating creates unstable atmospheric conditions by early-late afternoon (Dai 2001a; Dai et al. 2007). However, over the central U.S., the Tibetan Plateau and its east periphery, and other regions, moist convection and precipitation tend to occur from midnight to early morning as daytime convection is suppressed by large-scale atmospheric subsidence and due to other factors (Dai et al. 1999; Yu et al. 2007, 2014; Zhao et al. 2022). Over open oceans, precipitation tends to peak in early morning with a weaker diurnal amplitude, roughly out of phase with continental precipitation diurnal cycle (Dai 2001a; Dai et al. 2007). It is suggested that strong summer diurnal cycle over land could induce an out-of-phase diurnal cycle in surface convergence and atmospheric convection over nearby oceans (Dai and Deser 1999; Dai 2001a), thus contributing to the diurnal cycle of oceanic precipitation. Showery or convective precipitation, which is a major form of warm-season precipitation over both land and ocean (Dai 2001b), tends to peak 1–2 h later than total precipitation over most warm-season land areas (Dai 2001a), and satellite observations tend to capture mainly the diurnal phase of convective precipitation (Dai et al. 2007). During the cold season, total precipitation is dominated by non-showery precipitation (Dai 2001b), whose diurnal cycle is weak and tends to peak around 0600 local solar time (LST) over most land areas and from midnight to 0400 LST over many oceans (Dai 2001a).

In general, warm-season moist convection and precipitation in climate and weather models tend to start and peak too early compared to observations, often soon after noon (Dai and Trenberth 2004; Dai 2006; Lee et al. 2007a; Flato et al. 2013), although there are some improvements in the latest CMIP6 models (Lee and Wang 2021; Tang et al. 2021; Tao et al. 2023). Coarse model resolution, which fails to resolve land–ocean contrast around coasts and islands, and problems in convective initiation (or trigger function) and in coupling to surface heating, have been identified as some of the major factors contributing to the biases in model-simulated precipitation diurnal cycle (Dai and Trenberth 2004; Lee et al. 2008; Wang et al. 2015, 2020; Song and Zhang 2017, 2018; Wang and Hsu 2019; Xie et al. 2019; Cui et al. 2021; Lee and Wang 2021). The coarse resolution is also linked to the "drizzling" bias in climate models (Dai 2006; Chen et al. 2021), which may affect the simulated precipitation diurnal cycle as well. Regional models explicitly resolving convection without cumulus parameterization generally show improved diurnal cycles of convection and precipitation (Prein et al. 2015; Li et al. 2020; Scaff et al. 2020; Liu et al. 2022), which further indicates the role of cumulus parameterization in causing the diurnal biases in model-simulated precipitation and convection. Precipitation from atmospheric reanalyses can capture many of the large-scale diurnal variations, but often lack some of the small-scale or regional features (Chen et al. 2014; Hayden et al. 2023).

Most of the studies on cloudiness diurnal variations used satellite observations, which observe high clouds better than low clouds (e.g., Cairns 1995; Hahn et al. 1995; Rozendaal et al. 1995; Bergman and Salby 1996; Kondragunta and Gruber 1996; Wylie and Woolf 2002; Stubenrauch et al. 2006; Noel et al. 2018; Chepfer et al. 2019). In contrast, relatively few studies analyzed surface cloud observations, which are more reliable for low clouds than high clouds (Hahn et al. 1995). Three-hourly cloud data from the International

Satellite Cloud Climatology Project (ISCCP; Rossow & Schiffer 1991) show that low-level clouds tend to peak from noon to 03PM LST over most continental areas and around 02–05 AM LST over many oceans within 40° N/S, while mid-high clouds tend to peak from late afternoon to evening over most ocean and land areas (Bergman and Salby 1996). Surface cloud observations also confirm that maximum cloud cover occurs at night over open oceans, while there are more clouds during daytime than at night over land (Hahn et al. 1995). Clearly, such diurnal variations will have major impacts on shortwave and longwave radiation; thus, their representation in climate models is of great concern. Current climate models capture the observed cloud diurnal variations reasonably well over the oceans, but over land they show excessive clouds at night and too few clouds during the day without the early afternoon peak (Chen et al. 2022). In addition, high climate sensitivity in latest climate models is linked to strong positive extratropical cloud feedback (Zelinka et al. 2020).

Relatively few studies have examined the diurnal variations in convective available potential energy (CAPE) and convective inhibition (CIN), PBLH and surface fluxes on a global scale. Dai et al. (1999) used 6-hourly reanalysis data to show that CAPE over the U.S. peaks around 00 or 18 UTC (local afternoon). Estimates using in-situ soundings from a few locations seem to suggest a nighttime peak of oceanic CAPE (Bellenger et al. 2010) and an early afternoon peak of CAPE over land (Ratnam et al. 2013; Tang et al. 2016). Estimates of land PBLH using in-situ soundings and other measurements show an early afternoon peak (Liu and Liang 2010; Gu et al. 2020; Zhang et al. 2020; Guo et al. 2021). PBLH estimates from soundings from sparse oceanic field campaigns (Liu and Liang 2010) and twice-daily operational soundings from coastal and island stations (Gu et al. 2020) show higher PBLH around noontime than at night over many tropical and midlatitude oceans. Bulk formula-based estimates of surface sensible heat (SH) and latent heat (LH) fluxes using in-situ measurements from sparse locations over land show either a near noontime peak for both SH and LH fluxes over the central U.S. (Zhang and Klein 2010) or a peak around 1500 LST for SH fluxes over the Tibetan Plateau (Zhu et al. 2023).

In this study, I extend the analysis of Dai (2023) to examine the diurnal variations in precipitation and cloud cover in observations and ERA5, and also briefly analyze the diurnal variations in ERA5 buoyancy, boundary layer, and surface fluxes. ERA5 (Hersbach et al. 2020) provides hourly data for many surface and atmospheric fields; thus, it represents a valuable resource for studying the diurnal cycle. However, precipitation, clouds and the other variables analyzed here are not directly constrained by observations in ERA5; thus, their usefulness needs to be validated. Previous studies have evaluated the diurnal cycle in ERA5 precipitation over specific regions, e.g., eastern China where ERA5 reproduces the late-afternoon peak with an excessive amplitude (Qin et al. 2021), the Tibetan Plateau (Chen et al. 2023b) where ERA5 precipitation peaks two early, and the maritime continent and the Amazon where ERA5 precipitation peaks a few hours early than satellite observations (Hayden et al. 2023). Some regional studies also examined diurnal variations in ERA5 clouds, e.g., over western central Africa (Dommo et al. 2022) and the Tibetan Plateau (Cao et al. 2022; Zhao et al. 2023b). However, few studies have examined the diurnal variations in ERA5 precipitation or cloud cover over the globe, which is necessary for revealing any planetary-scale features, such as the migrating wave-number 1 or 2 mode seen in pressure and temperature fields (Dai 2023). The goal here is to provide a comprehensive global analysis of the diurnal variations in precipitation and cloud cover in observations and ERA5. The results should improve our knowledge of the diurnal cycles in precipitation and clouds over the globe and their representation in ERA5. The diurnal results can also be used to evaluate climate model simulations.

2 Data and method

The observational data for precipitation frequency and cloud cover were derived from the 3-hourly weather reports from over 15,000 weather stations on land (including many islands) and ship and buoy observations over oceans during 1976–2007 (1975–1997 for occurrence frequency for non-drizzle, showery and non-showery precipitation as in Dai 2001a). These surface weather reports were previously used by the author to derive precipitation frequency over the globe (Dai 2001a, b) and cloud amount (Dai et al. 2006). For comparison, I also analyzed 30-min precipitation data from June 2000–April 2021 (on 0.1° grid, averaged onto 1° grids) from the IMERG v06B dataset (Huffman et al. 2021), which was derived from satellite observations and scaled to match rain-gauge-based monthly precipitation amount. Due to the poor vision under dark night without moonlight, the dark-night cloud amount from surface observations may be underestimated, leading to slight underestimation (by ~ 2%) of the mean cloud amount and significant impact on its diurnal cycle (Hahn et al. 1995). Here, I re-processed the surface observations of total, low and middle cloud amount (excluding biased reports from automated measurements, Dai et al. 2006) from 1976 to 2007 to exclude the biased reports during dark nights, which are defined as the nighttime with R (relative lunar illuminance) ≤ 0.11 when the Sun is more than 9° below the horizon following Hahn et al. (1995). I found that excluding the dark-night reports has a significant impact on cloud diurnal cycle and bring it closer to that seen in satellite observations, consistent with Hahn et al. (1995).

High cloud amount can be derived from the total, low and middle cloud amounts using random overlapping but is less reliable. For comparison, I also analyzed the 3-hourly total, low, middle and high cloud amount data from the International Satellite Cloud Climatology (ISCCP, Rossow & Schiffer 1991) H-series product on 1° grids from July 1983 to June 2017 (Young et al. 2018; https://www.ncei.noaa.gov/products/climate-data-records/cloud-properties-isccp). I also analyzed hourly data for cloud amounts and surface radiative fluxes from CERES SYN1deg_Ed4A dataset on 1° grids from March 2000 to December 2022 (Doelling et al. 2016; https://ceres.larc.nasa.gov/data/), which was derived from various satellite observations using algorithms similar to that for ISCCP D2 for clouds and calculated using radiative transfer and top-of-the-atmosphere flux measurements for surface fluxes. Cloud diurnal anomalies from CERES were found to be noisier than those seen in ISCCP and surface observations and thus are not discussed below. I used the monthly-averaged hourly data for total, convective and large-scale precipitation, total, low, middle and high cloud cover, PBLH, CAPE, CIN, and surface energy fluxes from ERA5 (Hersbach et al. 2020) on 1° grids from 1979 to 2020 to derive their mean diurnal variations. CAPE and CIN estimates using twice-daily homogenized radiosonde data from Chen and Dai (2023) are compared with the ERA5 data. However, PBLH (Guo et al. 2021) data are unavailable over most of the globe; thus, I only analyzed PBLH from ERA5 with comparisons to results from some recent observational studies.

I first averaged the observational and ERA5 data over their data periods to derive the long-term mean diurnal variations. The differences in the averaging time periods among the different datasets should not impact the results significantly as the long-term mean diurnal cycle is relatively stable. I then mapped out the diurnal anomalies (relative to the daily mean) for 00, 06, 12 and 18Z (or UTC) to examine their global patterns and any migrating features. The local diurnal anomalies were also averaged spatially for each LST hour to derive regional mean composite diurnal cycle for three latitude zones for land and ocean separately: the northern extratropics (25° N–70° N), tropics (25° S–25° N), and southern extratropics (25° S–50° S). For example, an anomaly for 03Z at 15° E is for 04 LST and would be averaged with the anomaly for 00Z at 60° E (which is also for 04 LST). Observations not exactly at an LST hour is assigned to the nearest hour before the averaging. Furthermore, as in our previous studies (Dai et al. 1999; Dai 2001a; Dai and Trenberth 2004), the long-term mean diurnal curve at each grid box was fitted with the diurnal (24 h, S1) and semidiurnal (12 h, S2) harmonics to quantify their contributions to the diurnal variations (see eqs.1–2 in Dai and Wang 1999). As an example, Fig. 1 shows the fitting to the hourly data from 00-24 h LST of the diurnal variations in ERA5 precipitation, total cloud cover, CAPE and PBLH at a grid box in the Southeast U.S. It shows that the diurnal component S1 dominates the diurnal variations for all the four variables, although the semidiurnal component S2 also has significant contributions that improve the fitting substantially. In other words, while the composite diurnal anomalies tend to have only one peak, their diurnal variations do not exactly follow the S1 harmonic, and the inclusion of the S2 harmonic significantly improves the fitting. As in Dai (2023), here diurnal variations or anomalies in all the figures and discussions refer to the actual deviations from the daily mean (black dots in Fig. 1), not the S1 or S1 + S2 component, and the diurnal amplitude refers the maximum minus daily mean difference. The use of daily-mean sea surface temperatures (SST) as the lower boundary condition in ERA5 suppresses near-surface

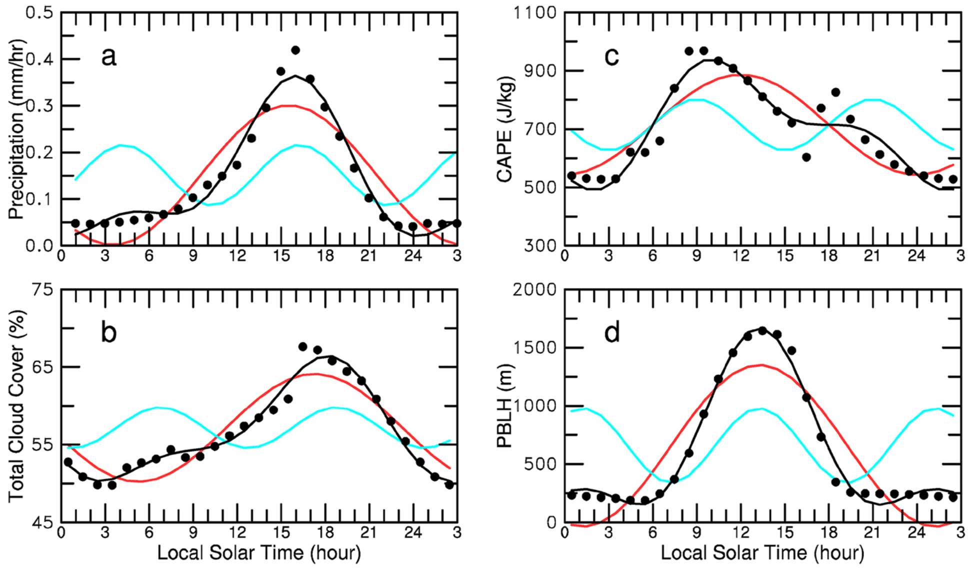

Fig. 1 Long-term (1979–2020) averaged diurnal variations (dots) at a S.E. US grid box (83° W, 32° N) in ERA5 **a** precipitation, **b** total cloud cover, **c** CAPE, and **d** PBLH. The fitted 24-h (red line) and 12-h (blue line) harmonics and their sum (black line) are also shown

diurnal cycle in air temperature and other fields (Dai 2023), and it likely also dampens the diurnal variations in oceanic PBLH, CAPE, CIN and surface heat fluxes, as shown previously (e.g., Bellenger et al. 2010).

3 Results

3.1 Diurnal variations in precipitation

Before evaluating the diurnal cycle, we will first examine how well ERA5 reproduces the precipitation climatology. Figure 2 compares the 1979–2020 mean precipitation for December–January–February (DJF) and June–July–August (JJA) from ERA5 and GPCP v2.3 (Adler et al. 2017; http://eagle1.umd.edu/GPCP_CDR/Monthly_Data/), which is derived mainly from rain-gauge data over land and satellite observations over ocean. Given that ERA5 assimilated precipitation observations only over the contiguous USA since about 2009 (Hersbach et al. 2020), it is remarkable that ERA5 reproduces the observed precipitation patterns well over the globe, with a spatial pattern correlation of 0.97 with the GPCP data for both DJF and JJA. Noticeable wet biases exist, however, in the tropics (especially over the inter-tropical convergence zones) and some dry biases are seen over Europe and northwestern Asia in DJF. Given the considerable differences in current estimates of oceanic precipitation amount (with the GPCP on the lower side of the range, Dai 2006), the mean biases shown in Fig. 2e–f over oceans is acceptable. On the other hand, ERA5 hourly precipitation was found to overestimate the frequency but underestimate the intensity over eastern China (Qin et al. 2021), although the comparison of rain-gauge station data with ERA5 0.25° grid-box mean precipitation in Qin et al. (2021) may have exacerbated these biases since estimated precipitation frequency (intensity) increases (decreases) with the averaging area (Chen and Dai 2018).

Figure 3 compares the diurnal anomalies in JJA precipitation frequency from surface weather reports and precipitation amount from IMERG and ERA5 at 00, 06, 12 and 18Z. Unlike surface temperature and pressure (Dai 2023), there exist no clear global wave patterns in the precipitation anomalies; the land–ocean contrast seems to dominate together with many localized features (e.g., over the central U.S. and Southeast Asia). In general, land precipitation tends to peak in the afternoon (i.e., to the right side of the vertical blue line in Fig. 3), while ocean precipitation peaks in the early morning. There exists some general consistency between the IMERG and surface observed anomalies, although considerable differences exist among them. The ERA5 precipitation diurnal anomalies compare better with the surface observations than IMERG, although large differences exist (e.g., over the Southern Ocean where surface observations are sparse). ERA5 precipitation diurnal anomalies over northern

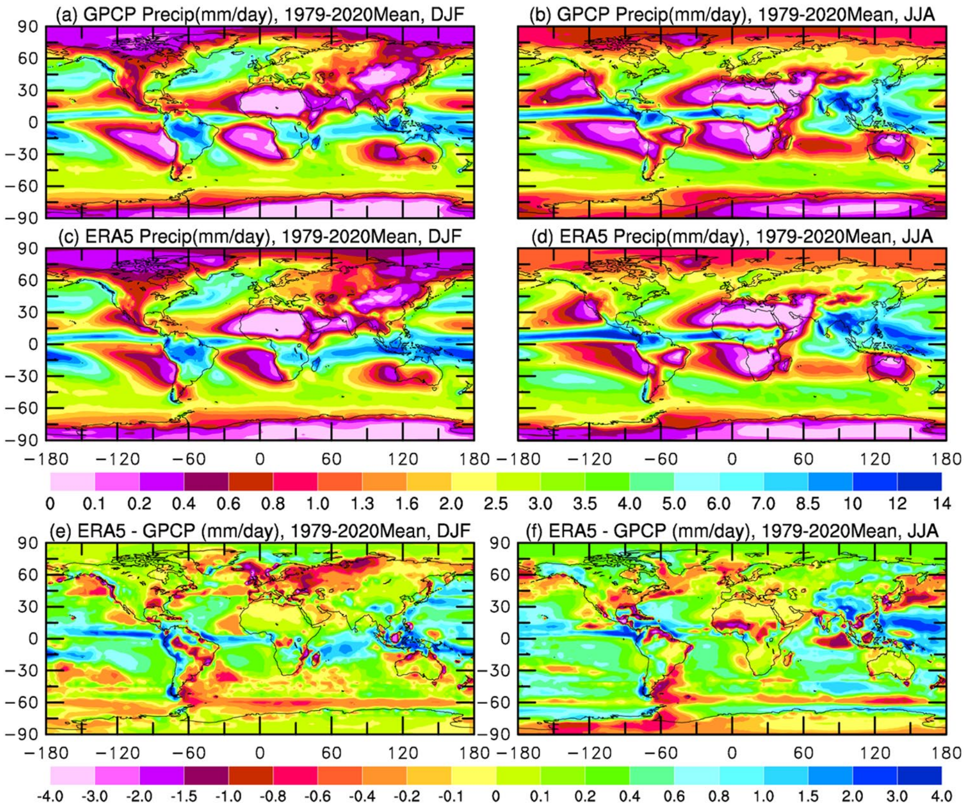

Fig. 2 Long-term (1979–2020) mean DJF and JJA precipitation from **a**, **b** GPCP v2.3 and **c**, **d** ERA5, and **e, f** the ERA5 minus GPCP precipitation difference in units of mm/day. The area-weighted pattern correlation between **a** and **c** and between **b** and **d** is both 0.97

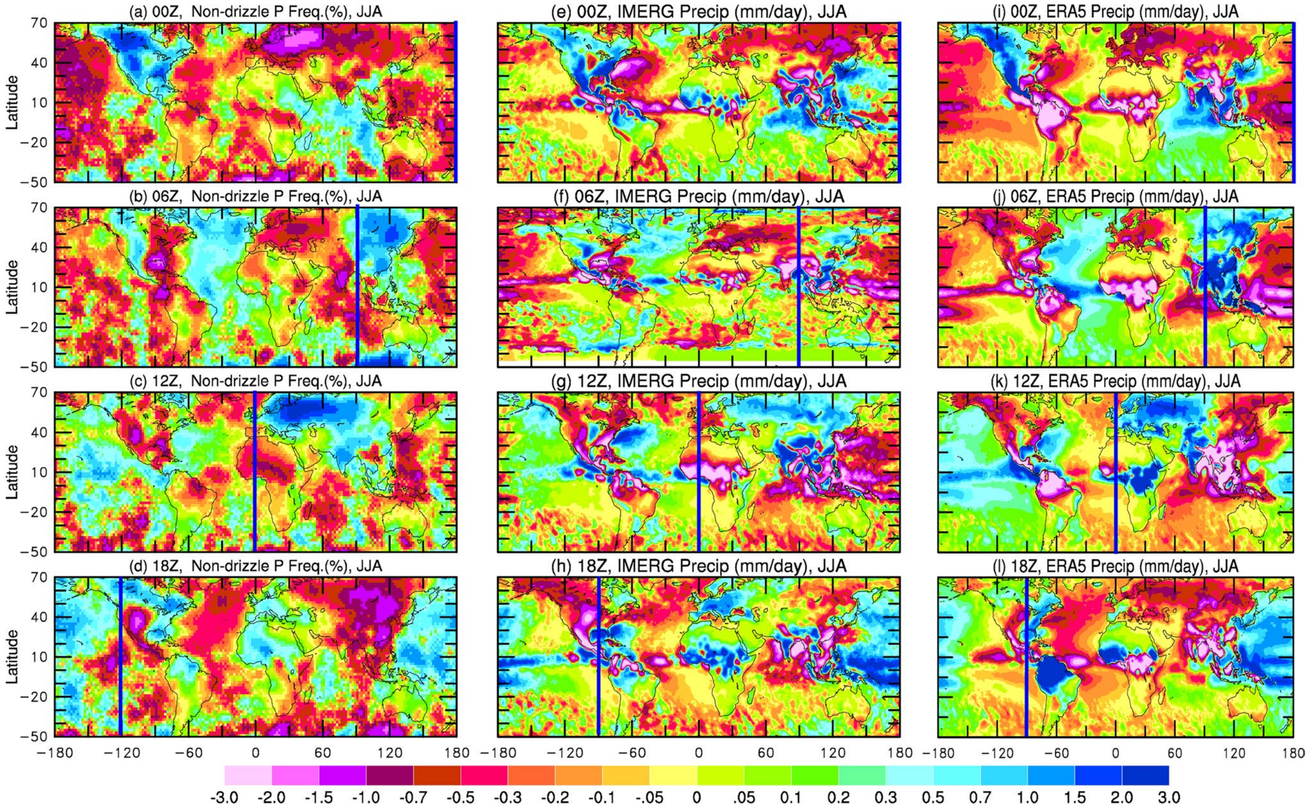

Fig. 3 Distributions of the long-term mean diurnal anomalies of JJA precipitation **a–d** frequency (in % of time, multiplied by 0.5 to use the same color scale, with spatial smoothing to reduce sampling noise) and **e–l** amount (in mm/day) at **a**, **e**, **i** 00Z (or UTC), **b**, **f**, **j** 06Z, **c**, **g**, **k** 12Z, and **d**, **h**, **l** 18Z from **a–d** surface weather reports during 1975–1997, **e–h** IMERG satellite observations averaged from 6/2000–4/2021, and **i–l** ERA5 reanalysis averaged over 1979–2020. The vertical blue line indicates the location of the Sun, with the region to the left (right) side of the line is in the morning (afternoon) hours

South America, central Africa and South Asia appear to be either too strong or slightly out-of-phase with both the surface and IMERG data (Fig. 3).

The land–ocean diurnal phase contrast becomes more obvious in zonally averaged composite diurnal curves, which show that warm-season precipitation peaks around 16–17 LST over land but around 05–06 LST over ocean (Fig. 4a–c), consistent with previous estimates (e.g., Dai 2001a; Dai et al. 2007). For the cold season (i.e., DJF for 25° N–70° N and JJA for 25° S–50° S), precipitation diurnal variations are small in observations (Fig. 4a–c). The IMERG satellite observations capture these broad features, with a sharper and slightly delayed peak (around 17 LST) over land and oceanic peak around 06LST (Fig. 4d–f). ERA5 captures the general phase contrast between land and ocean for warm-season precipitation, with a stronger amplitude and an earlier peak around 14–16 LST over land (Fig. 4g–i). Over oceans, ERA5 precipitation diurnal variations are comparable to IMERG, with a slightly stronger peak around 03–05 LST, about 1 h earlier than that in surface and satellite observations (Fig. 4). This is somewhat surprising given that ERA5 does not have a diurnal cycle in its specified SST, leading to weak diurnal variations in surface air temperature and humidity fields over oceans (Dai 2023). These results suggest that oceanic precipitation diurnal cycle is not tightly coupled to near-surface diurnal variations but is more controlled by free-tropospheric processes such as large-scale land–ocean diurnal circulation and local radiative cooling (Gray and Jacobson 1977; Dai 2001a). This is in sharp contrast to land precipitation diurnal cycle, which is greatly influenced by surface daytime heating induced by solar radiation (Dai et al. 1999; Liang et al. 2004).

The diurnal cycle in ERA5 convective precipitation is also comparable to surface observations of showery precipitation, with a slightly earlier peak around 15 LST (compared with 16–17 LST in surface observations) and a stronger amplitude for warm-season precipitation over land (Fig. 5). The excessive amplitude, as well as the earlier phase, in convective precipitation is the main contributor to the excessive amplitude in ERA5's total precipitation diurnal anomalies (Fig. 4), as its large-scale precipitation has smaller diurnal amplitudes and different phases (Fig. 6). Warm-season convective precipitation over oceans in ERA5 also peaks slightly earlier (by ~ 1 h) around 03–05 LST than surface

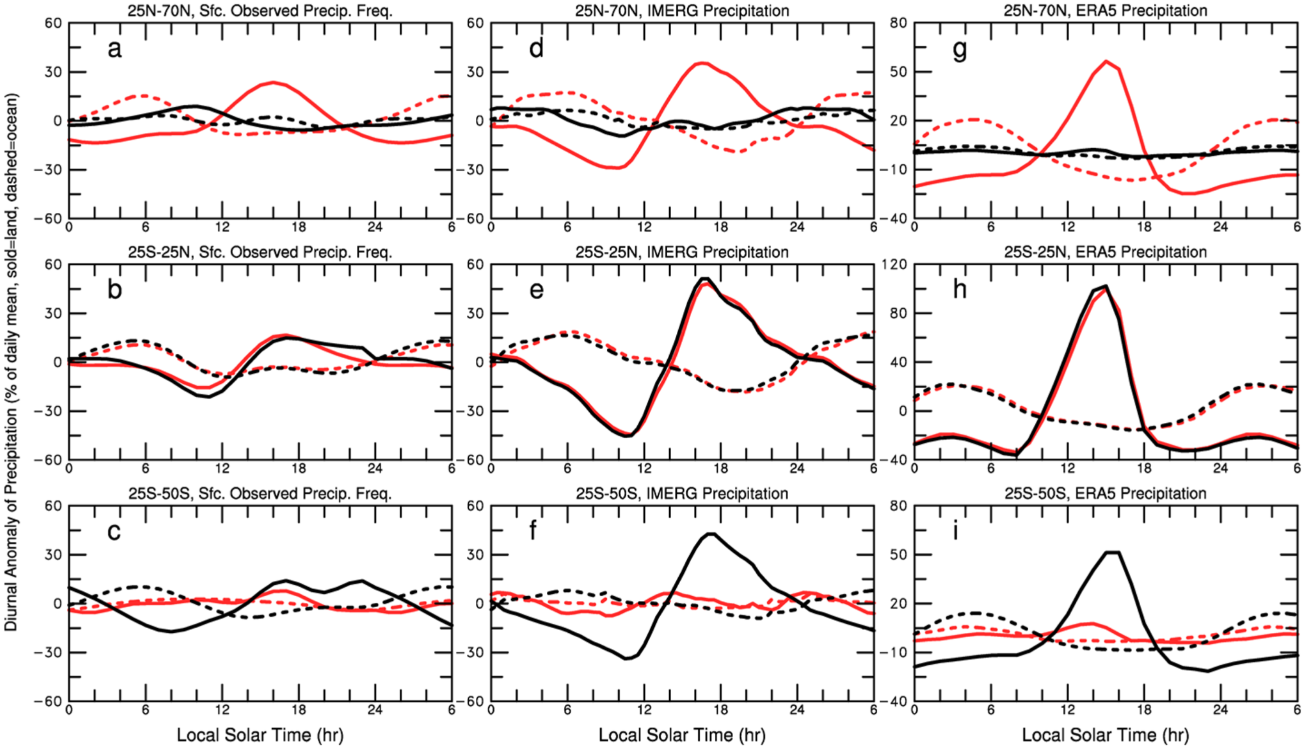

Fig. 4 Mean diurnal cycles of precipitation **a**–**c** frequency and **d**–**i** amount averaged over land (solid lines) and ocean (dashed lines) in December-January–February (DJF, black lines) and June-July–August (JJA, red lines) within the **a**, **d**, **g** northern extra-tropics (25° N–70° N), **b**, **e**, **h** tropics (25° S–25° N), and **c**, **f**, **i** southern extra-tropics (25° S–50° S) from **a**–**c** surface weather reports during 1975–1997 (Dai 2001a, b), **d**–**f** IMERG averaged from 6/2000 to 4/2021, and **g**–**i** ERA5 reanalysis hourly data averaged from 1979 to 2020 (note the larger y-axis scale on **g**–**i**). The mean composite diurnal cycle was derived by first converting the UTC time into local solar time (LST = UTC + longitude/15, where longitude varies from − 180 to + 180, negative longitudes for the western hemisphere), and then averaging the diurnal anomalies (relative to the long-term mean of the daily mean) at each nearest LST hour over all the land or ocean grid boxes within the latitudinal zone and then expressed in percentage of the daily mean of the region

observations, with slightly stronger percentage amplitudes (Fig. 5). Both DJF convective precipitation over 25° N–70° N land and JJA convective precipitation over 25° S–50° S land show a moderate peak around 15–16 LST in surface observations (Fig. 5a, c), suggesting that cold-season convective precipitation does have a weak diurnal cycle that peaks slightly earlier than that for the warm season. ERA5 also shows a moderate early afternoon peak (around 14 LST) in cold-season land convective precipitation (Fig. 5d, f), while it produces very similar diurnal cycles for both DJF and JJA for both convective and total precipitation for the tropics (Figs. 4h, 5e). The DJF versus JJA differences for 25° S–25° N are also small in IMERG (Fig. 4e) but noticeable in surface observations (Figs. 4b, 5b).

Non-showery precipitation from surface observations and large-scale precipitation from ERA5 (Fig. 6) both show a moderate diurnal cycle with a morning peak and an evening minimum. Over 25° N–70° N, ERA5 captures the observed non-showery precipitation diurnal cycle in JJA very well for both land and ocean, with a comparable amplitude (~ 15% of the daily mean) and a slightly delayed (by ~ 1 h) peak around 07–08 LST over land and 04–05 LST over ocean (Fig. 6d). DJF land non-showery precipitation shows a weak peak around 10 LST in surface observations, while ERA5 DJF large-scale precipitation shows little diurnal variation over 25° N–70° N (Fig. 6a, d). In the tropics, ERA5 large-scale precipitation shows a plateau with elevated amounts from 04–16 LST and a minimum around 18–22 LST over land, and a weak peak around 04 LST over ocean (Fig. 6e); while tropical non-showery precipitation from surface observations shows a weak peak around 07 LST except DJF land, which peaks around 02–04 LST (Fig. 6b). Over 25° S–50° S, surface observations show little diurnal variation in non-showery precipitation (Fig. 6c), while ERA5 shows a moderate morning peak for DJF large-scale precipitation around 09 LST over land and 05 LST over ocean (Fig. 6f).

Figure 7 compares the amplitude (i.e., the deviation from the daily mean) and phase (expressed as the LST of the peak) of the estimated diurnal harmonic S1 in DJF and JJA precipitation from surface observations and ERA5. In general, the S1 has an amplitude of ~ 20 to 50% (less than 20%) of the daily mean over most land and oceans during the

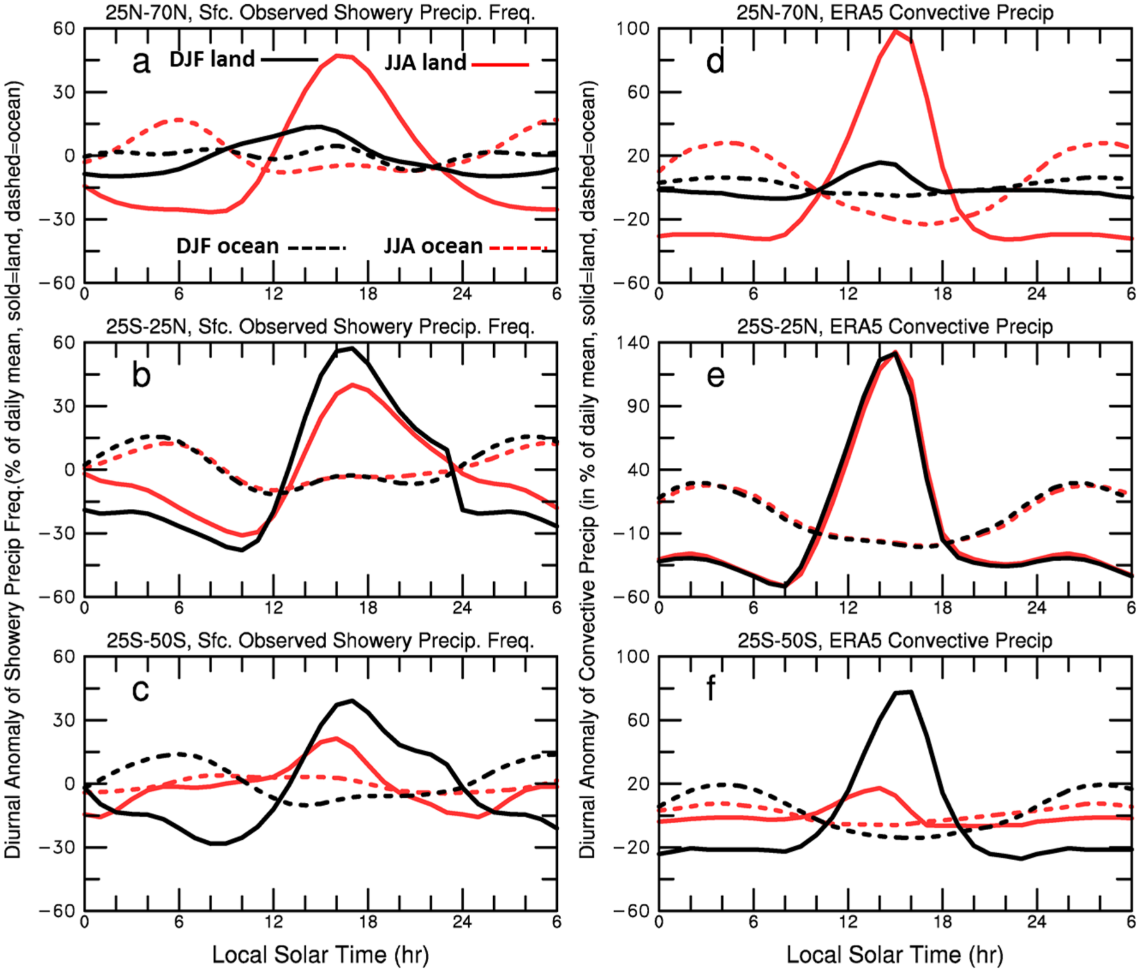

Fig. 5 Same as Fig. 4 but for diurnal anomalies (in % of the daily mean) for **a**–**c** showery precipitation frequency from surface observations (1975–1997 mean) and **d**–**f** convective precipitation from ERA5 (1979–2020 mean). Note the larger y-axis scale on **d**–**f**

warm (cold) season (Fig. 7a, b), and peaks from 14–20 LST in JJA and around 06–10 LST in DJF over most Northern Hemisphere land in surface observations (Fig. 7e, f), consistent with previous estimates (e.g., Dai 2001a; Dai et al. 2007). The phase over Southern Hemisphere land is noisy likely due to stronger influences from the oceans, but it tends to peak around 18–20 LST over many areas in Africa and South America in DJF (Fig. 7f). The estimated S1 in ERA5 total precipitation tends to have a stronger (weaker) amplitude over low-latitude land (mid-high latitudes) than surface observations (Fig. c–d), and the phase tends to be a couple of hours earlier than that in surface observations over both land and ocean, although the land–ocean phase contrast is well captured in ERA5 (Fig. 7g, h).

The estimated S1 of warm-season showery precipitation tends to peak from late afternoon to early evening (16–20 LST) over most land and around 04–08 LST over most ocean in surface observations (Fig. 8a, b), which are 1–2 h later than that for total precipitation over many land areas (Fig. 7e, f), consistent with previous estimates (e.g., Dai 2001a; Dai et al. 2007). The S1 of ERA5 convective precipitation (Fig. 8c, d) has a phase similar to that for its total precipitation for the warm season (Fig. 7g, h) and it is a couple of hours earlier than that for observed showery precipitation (Fig. 8a, b). In contrast, the non-showery or large-scale precipitation tends to peak in the morning (around 06–10 LST) over most land areas and many oceans in both observations and ERA5 (Fig. 8e–h), although the phase is noisy over the oceans partly due to its weak amplitude (Fig. 6).

The phase of the estimated S1 in IMERG total precipitation is closer to that for showery precipitation (Fig. 9e–h) than for total precipitation (Fig. 7e, f) from surface observations. This suggests that satellite observations capture mainly convective precipitation (and clouds), leading to a late afternoon to early evening (17-20 LST) peak over most warm-season land (Fig. 9g, h), as noticed previously (Dai et al. 2007), although Tan et al. (2019) found a smaller phase delay in IMERG v06 compared with a ground-based

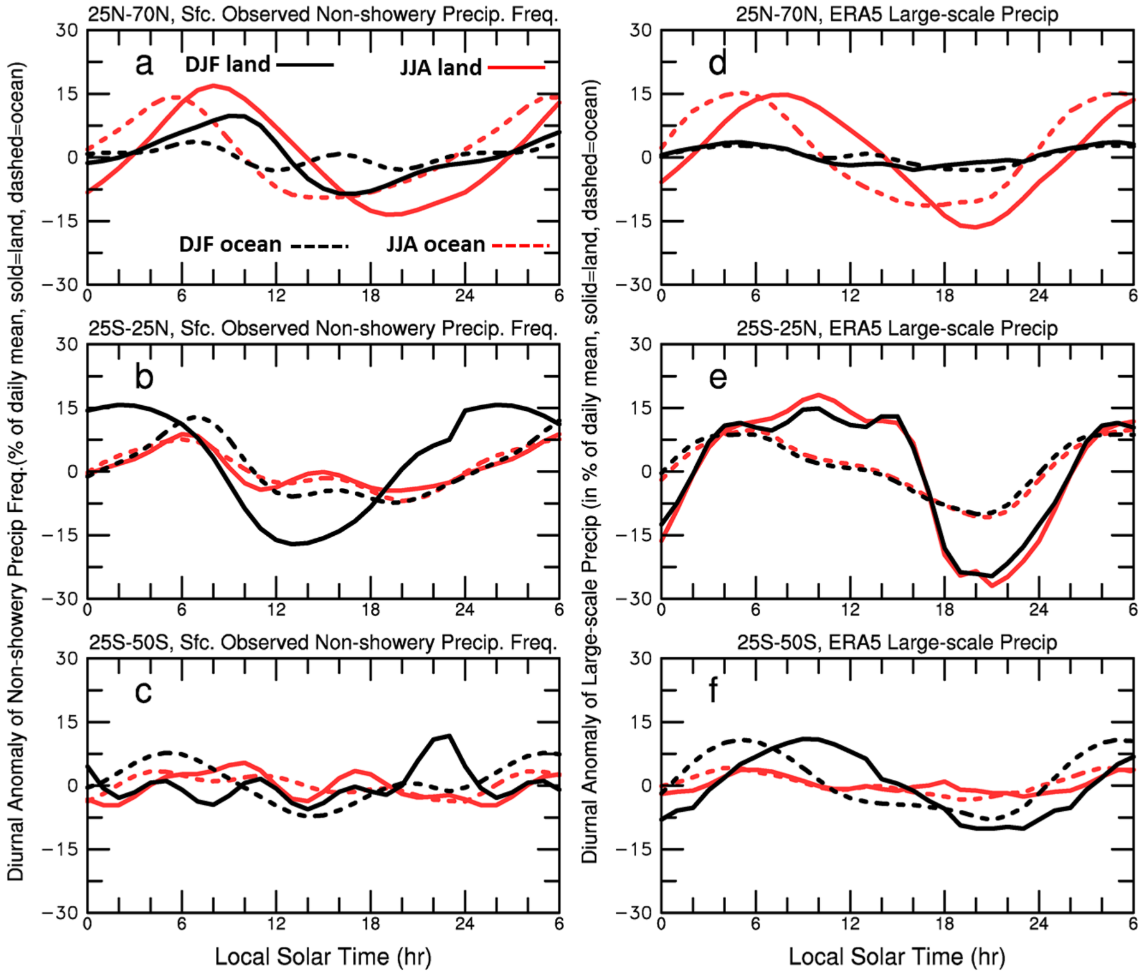

Fig. 6 Same as Fig. 4 but for diurnal anomalies (in % of the daily mean) for **a**–**c** non-showery precipitation frequency from surface observations (1975–1997 mean) and **d**–**f** large-scale precipiation from ERA5 (1979–2020 mean)

multi-sensor product over the U.S. The S1 amplitude in IMERG precipitation is comparable to that in surface observations, with slightly lower amplitudes over some midlatitude oceans (Figs. 9a–d, 7a, b). Thus, the IMERG data capture the diurnal cycle of mainly convective precipitation with a slightly delayed (by ~ 2 h) phase compared with surface observations of total precipitation over many warm-season land areas. The IMERG's S1 phase over low-midlatitude oceans is around 04–08 LST (Fig. 9g, h), which is comparable to that in surface observations (Figs. 9e, f, 7e, f).

3.2 Diurnal variations in cloud cover and cloud base height

Clouds reflect sunlight during the day and absorb and re-emit longwave radiation back to Earth's surface; thus, diurnal variations in cloud cover and cloud base height, which affects cloud-base temperature and thus its emitted downward longwave radiation, can have large impacts on Earth's surface energy budget. ERA5 does not assimilate any observations of clouds (Hersbach et al. 2020); thus, how well ERA5 reproduces the observed cloud climatology deserves examination. Figure 10 compares the DJF and JJA total cloud amount averaged over recent decades from surface observations, two satellite products and ERA5. There are noticeable differences between the ISCCP and CERES satellite products, e.g., over the North Pacific, Southern Ocean, and Antarctica (Fig. 10c–f). The satellite products also show generally higher cloud amount than surface observations over the North Pacific, North Atlantic, Southern Ocean, and other oceanic regions (Fig. 10a–f). Outside the polar regions where surface observations are sparse and satellite observations are less reliable, ERA5 cloud cover (Fig. 10g, h) is remarkably comparable with the surface observations, especially given the differences among the observational datasets. For example, ERA5 captures the observed sharp cloudiness gradients over Africa, Southwest North America,

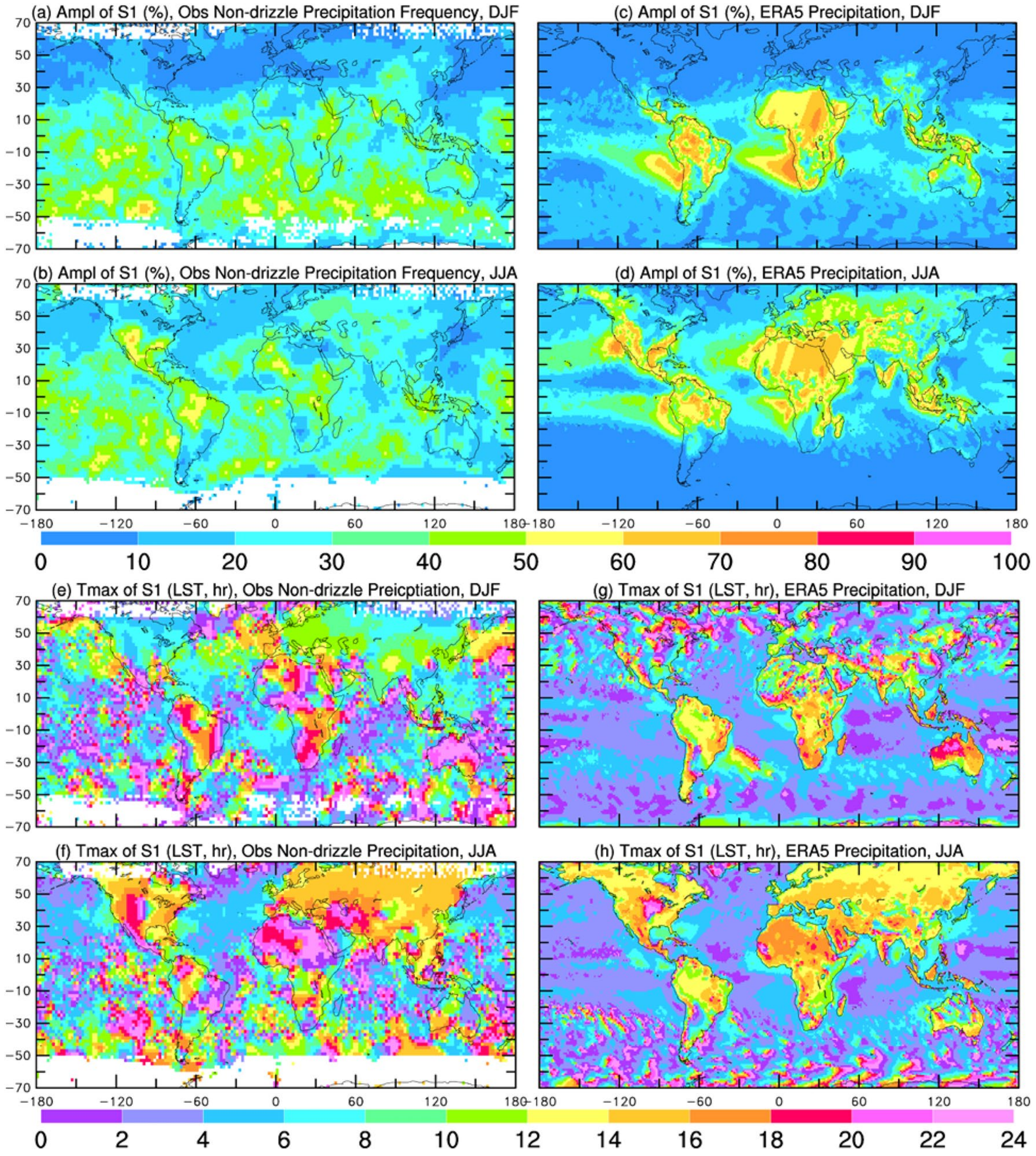

Fig. 7 **a–d** The amplitude (in % of daily mean) of the 24-h harmonic of the mean diurnal variations in **a**, **c** DJF and **b**, **d** JJA 3-hourly precipitation frequency from surface observations (left) and hourly precipitation amount from ERA5 (right). **e–h** Same as **a–d** but for the local solar time (LST, in hours) of the peak of the 24-h harmonic. The composite diurnal data were fitted with the 24-h harmonic for the 3 hourly surface observations and with the 12- and 24-h harmonics for the ERA5 hourly data. The 12-h harmonic is generally weaker than the 24 h harmonic. Amplitude values over 80% are largely due to small daily mean and thus were removed, and then small data gaps were infilled through spatial interpolation

and South America. ERA5 assimilated a lot of satellite radiance and other data of the troposphere since the 1980s, which may help its cloud simulation. However, I also examined ERA5 mean cloud amount for 1950–1978 when few satellite observations were available, and the 1950–1978 climatology (not shown) is still very similar to that shown in Fig. 10g, h. This suggests that the assimilation of recent satellite observations is not the key factor for ERA5 to produce realistic cloud cover over most of the globe.

Over the Arctic, ERA5 seems to produce too many clouds for both DJF and JJA with little seasonal variation, although satellites may underestimate cloud amount over Arctic sea ice as noticed previously (Liu et al. 2010; Yeo et al. 2022;

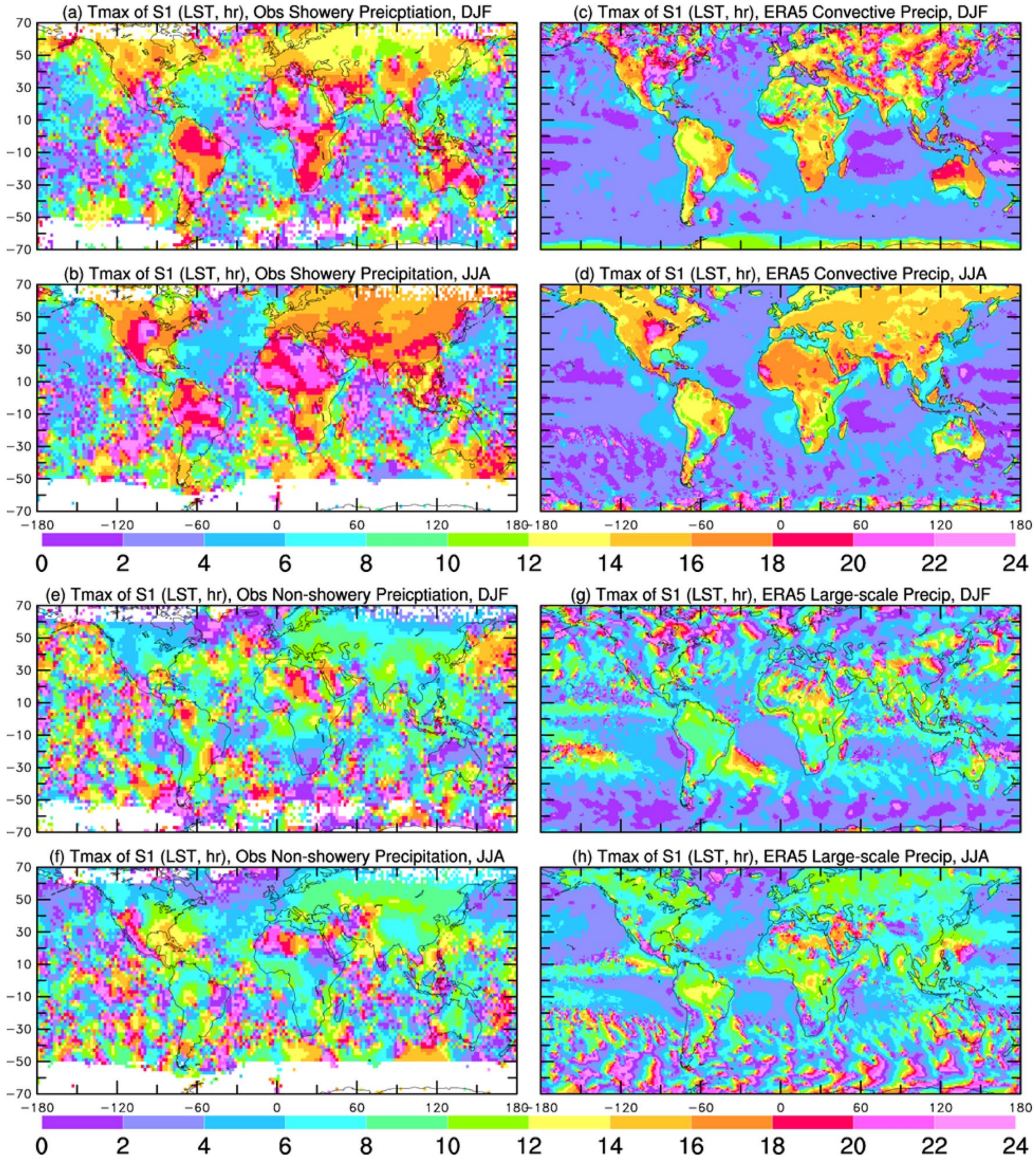

Fig. 8 **a**–**d** The local solar time (LST, in hours) of the peak of the 24-h harmonic of the mean diurnal variations in (left) showery precipitation frequency from surface observations and (right) ERA5 convective precipitation for **a**, **c** DJF and **b**, **d** JJA. **e**–**h** Same as **a**–**d** but for the phase of (left) surface observed non-showery precipitation frequency and (right) ERA5 large-scale precipitation for **e**, **g** DJF and **f**, **h** JJA

Jenkins et al. 2023). The two satellite products (especially ISCCP) significantly underestimate low cloud cover over most of the globe (except arid land areas) compared with surface observations and ERA5 (figure not shown). Since low clouds account for a large portion of the total cloud amount in surface observations and ERA5, especially over the central Arctic, it is possible that the satellite products may significantly underestimate Arctic total cloudiness. Given the lack of surface observations and possible underestimation of Arctic clouds by satellites, it is premature to conclude that ERA5 greatly overestimates cloud cover over the central Arctic. Over the Southern Ocean, where positive cloud feedback is linked to high climate sensitivity in models (Zelinka et al. 2020), both surface (sparse sampling in JJA) and satellite observations show high (> 80%) cloud cover, and ERA5 captures this high cloudiness band although its

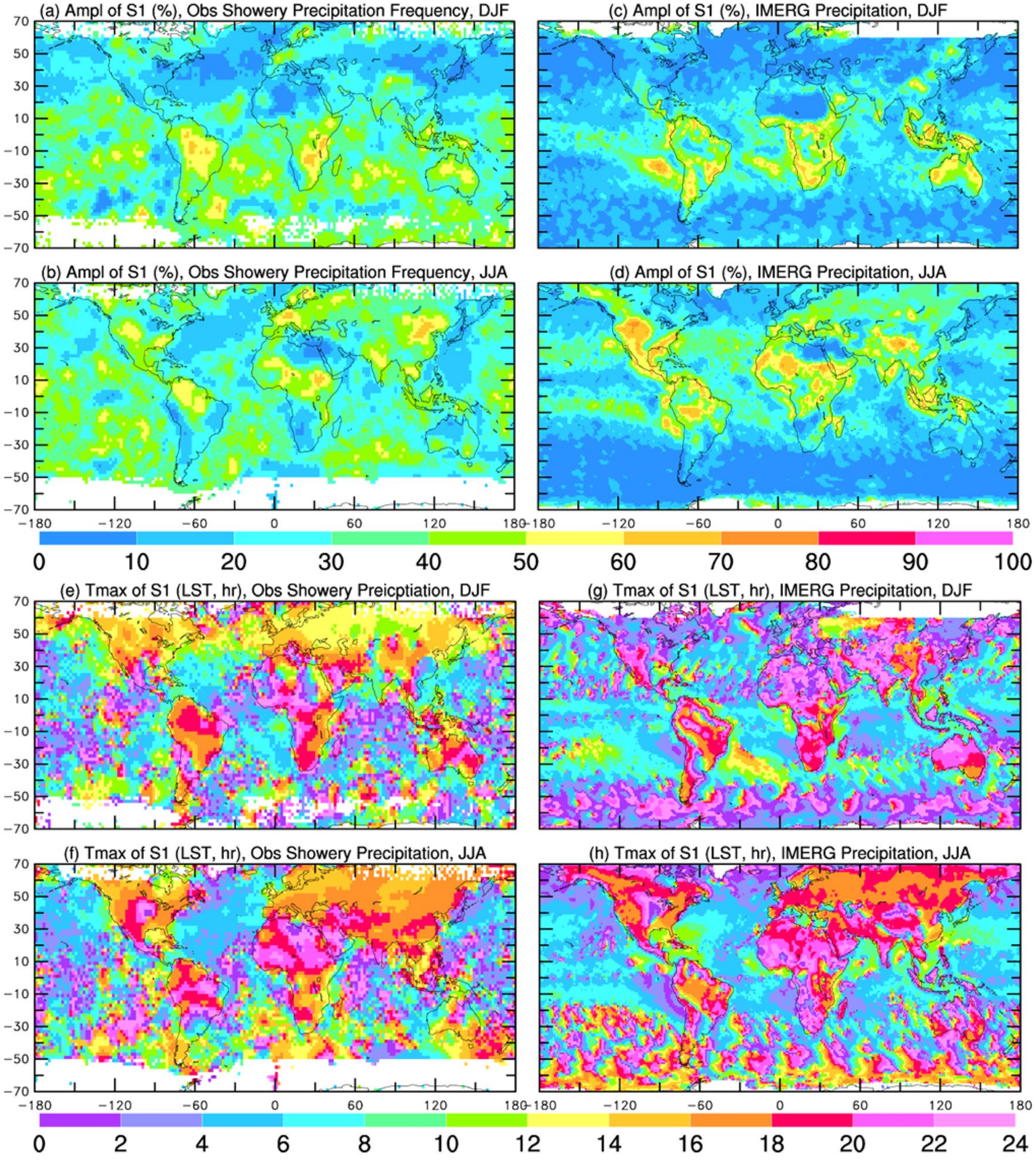

Fig. 9 **a**–**d** The amplitude (in % of daily mean) of the 24-h harmonic of the mean diurnal variations in **a**, **c** DJF and **b**, **d** JJA 3-hourly showery precipitation frequency from surface observations (left) and 30 min precipitation amount from IMERG (right). **e**–**h** Same as **a**–**d** but for the local solar time (LST, in hours) of the peak of the 24-h harmonic. The composite diurnal data were fitted with the 24-h harmonic for the 3-hourly surface observations and with the 12- and 24-h harmonics for the 30 min IMERG data. The 12-h harmonic is generally weaker than the 24 h harmonic. Amplitude values over 80% are largely due to small daily mean and thus were removed, and then small data gaps were infilled through spatial interpolation

DJF cloud cover is relatively low over the Southern Ocean (Fig. 10). Large amounts of low clouds (not shown) are also seen in ERA5 and warm-season surface observations over the Southern Ocean.

Figure 11 compares the long-term mean diurnal anomaly patterns of total cloud cover in JJA at 00, 06, 12 and 18Z from surface observations, ISCCP and ERA5. Without excluding the biased dark-night reports, total cloud cover from surface observations (figure omitted) would show a clear one-wave pattern with more (fewer) clouds during the day (at night). After excluding the dark-night reports, the westward migrating pattern (Fig. 11a–d) becomes noisy but more comparable to that for precipitation (Fig. 3a–d) and also to the ISCCP data (Fig. 11e–h). This increases our

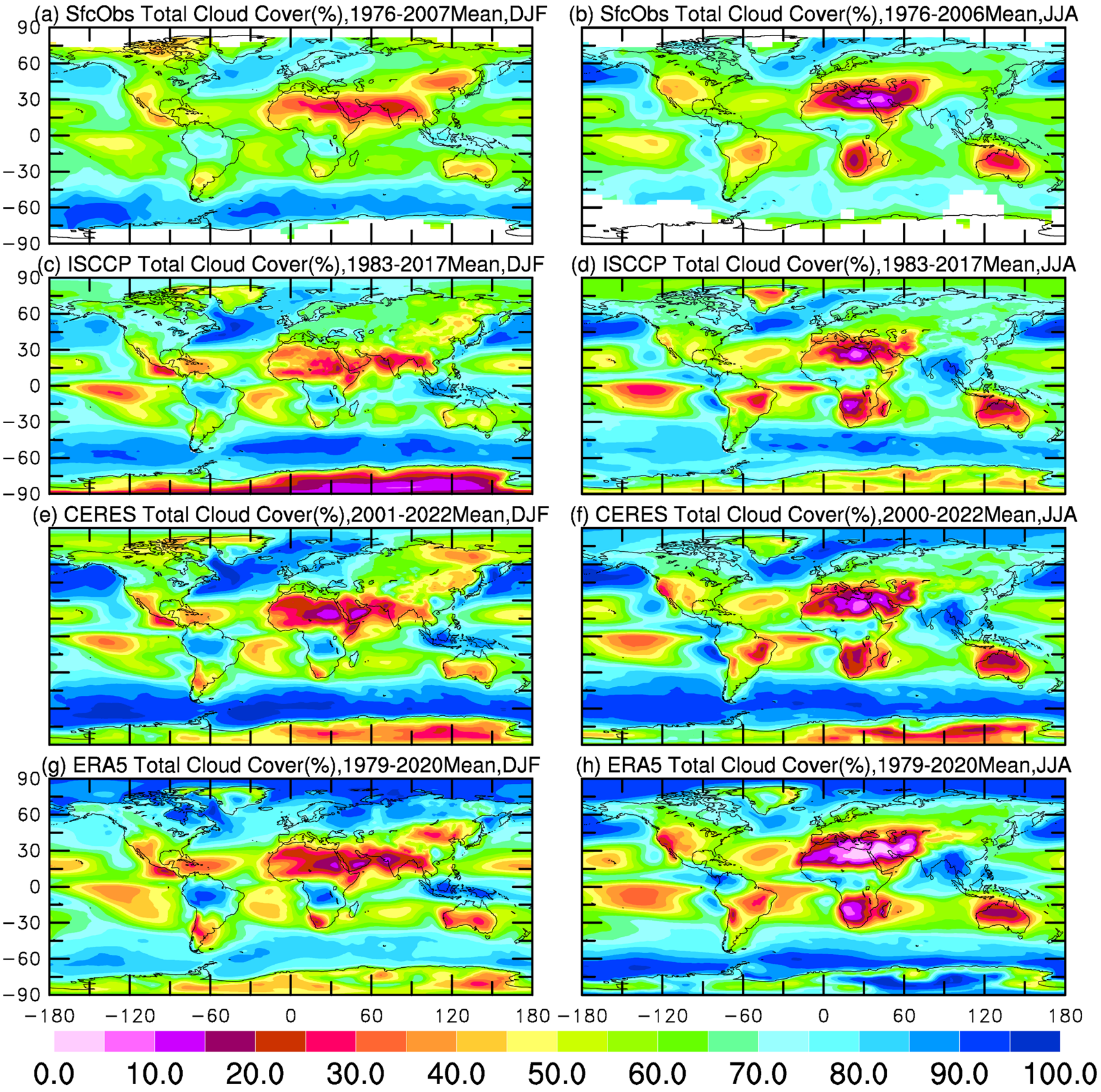

Fig. 10 Long-term mean total cloud cover (in % of the sky for surface observations or of the grid box for ISCCP and ERA5) for (left) DJF and (right) JJA from **a**, **b** surface observations (DJF 1976 to MAM 2007 mean; updated from Dai et al. 2006; dark-night reports were excluded), **c**, **d** ISCCP satellite observations (1983–2017 mean), and **e**, **f** CERES satellite observations (2001–2022 mean). **g**, **h** ERA5 reanalysis (1979–2020 mean). The area-weighted pattern correlation between **a** and **c** is r(**a**, **c**) = 0.90; other pattern correlations are r(**a**, **e**) = 0.94, r(**a**, **g**) = 0.82, r(**c**, **e**) = 0.96, r(**c**, **g**) = 0.87; r(**b**, **d**) = 0.91, r(**b**, **f**) = 0.96, r(**b**, **h**) = 0.96, r(**d**, **f**) = 0.95, and r(**f**, **h**) = 0.96

confidence in the cloud data (after removing the dark-night reports) as such a close association between cloudiness and precipitation is expected physically. The surface and satellite observations show that there are more clouds during daytime (nighttime) over land (ocean), as noticed previously (Hahn et al. 1995). ERA5 captures the broad patterns from observations, e.g., over western North America, Europe and South America at 00Z, and over North America, Asia and the eastern Atlantic at 06Z and 18Z (Fig. 11). Cloud cover (mainly from low clouds, Fig. 13) over the subtropical eastern Pacific (especially off Peru and Ecuador), which has been problematic in climate models (Dai and Trenberth 2004), peaks around 12Z (06 LST) and shows a minimum around 00Z (18 LST) in surface observations and ERA5 (Figs. 11 and 13).

The day-night differences in land cloud cover are shown more clearly in the zonal-mean averages (Fig. 12), which show a peak around 14 LST for warm-season clouds and elevated cloudiness from around 08–16 LST for the cold season in surface observations (Fig. 12a, c). Over tropical land, cloud cover shows two weak peaks around 07 and 16 LST (Fig. 12b). Over ocean, cloud diurnal variations are small, with slightly more clouds during early morning (Fig. 12a–c). The ISSCP clouds show sharper early afternoon peaks for both JJA and DJF over land than in surface observations,

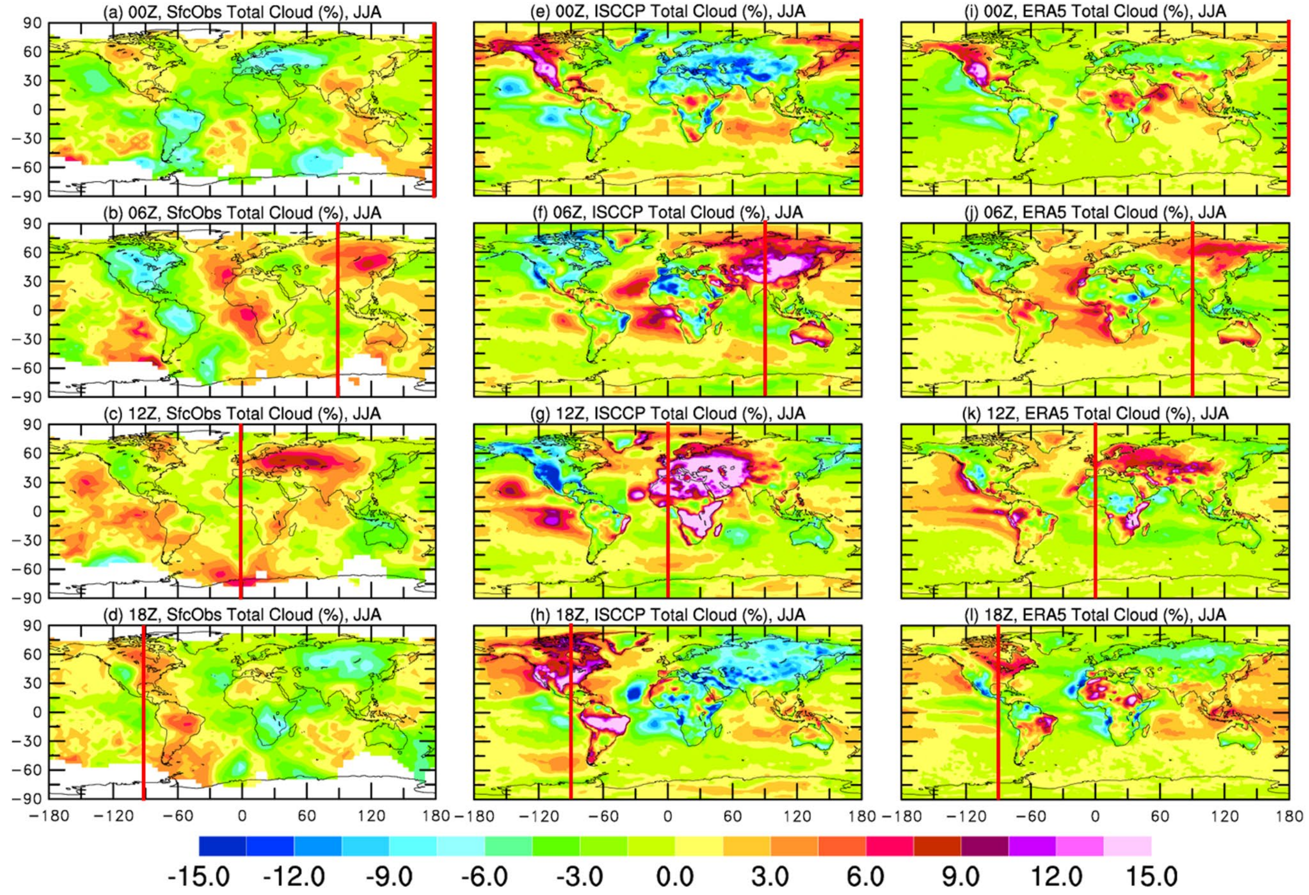

Fig. 11 Distributions of the long-term mean diurnal anomalies of JJA total cloud cover (in %) from **a**–**d** surface observations (1976–2006 mean, excluding dark-night reports), **e**–**h** ISCCP H-series (1983–2017 mean, and **i**–**l** ERA5 (1979–2020 mean) at **a**, **e**, **i** 00Z (or UTC), **b**, **f**, **j** 06Z, **c**, **g**, **k** 12Z, and **d**, **h**, **l** 18Z. The vertical red line indicates the location of the Sun, with the region to the left (right) side of the line is in the morning (afternoon) hours

while its marine clouds also show weak diurnal variations with slightly more clouds at night. In general, ERA5 cloud diurnal anomalies are more comparable to surface observations than ISCCP, which have too strong diurnal variations over land as shown by both Figs. 11 and 12.

The diurnal variations in total cloud cover result mainly from low clouds (Fig. 13), whose diurnal anomaly patterns resemble those in total clouds (Fig. 11), while diurnal variations in middle and high cloud cover are smaller (figure omitted). ERA5 low clouds show a strong diurnal cycle with a peak around 06 LST and a minimum in around 19 LST in the tropics and similar phases for the extratropical zones, while the peak is around 13–15 LST for warm-season low clouds over land in surface and satellite observations (Fig. 14). Figures 13 and 14 also show that the diurnal anomalies in ISCCP low clouds are too strong over land compared to surface observations, which are most reliable for low clouds. I recognize that the definitions of low clouds may differ somewhat among the three datasets; nevertheless, it is likely that ISCCP overestimates land low-cloud diurnal variations, which leads to its overestimation of total cloud diurnal variations over land. On the other hand, the phase biases in ERA5 low clouds (Fig. 14) likely have contributed to its biases in total clouds, especially for the tropics (Fig. 12).

Figure 15 shows the estimated amplitude and local time of the peak of the 24-h harmonic (S1) of the long-term averaged diurnal variations in total cloud cover for DJF and JJA from surface and satellite observations, and ERA5. Consistent with the anomaly maps (Fig. 11) and zonal averages (Fig. 12), Fig. 15a–d show that the cloudiness diurnal amplitude is strongest over land (especially warm-season land) and the marine stratus regions in the subtropical eastern Pacific and Atlantic, where it can reach 4–9% of the sky in surface observations and 10–20% in ISCCP. The ERA5 amplitude is generally comparable to surface observations, except for some overestimation over some areas in Africa and North America (for JJA) and some coastal regions and underestimation over extratropical oceans in the cold season (Fig. 15e, f). The estimated peak is around 10–14 LST in

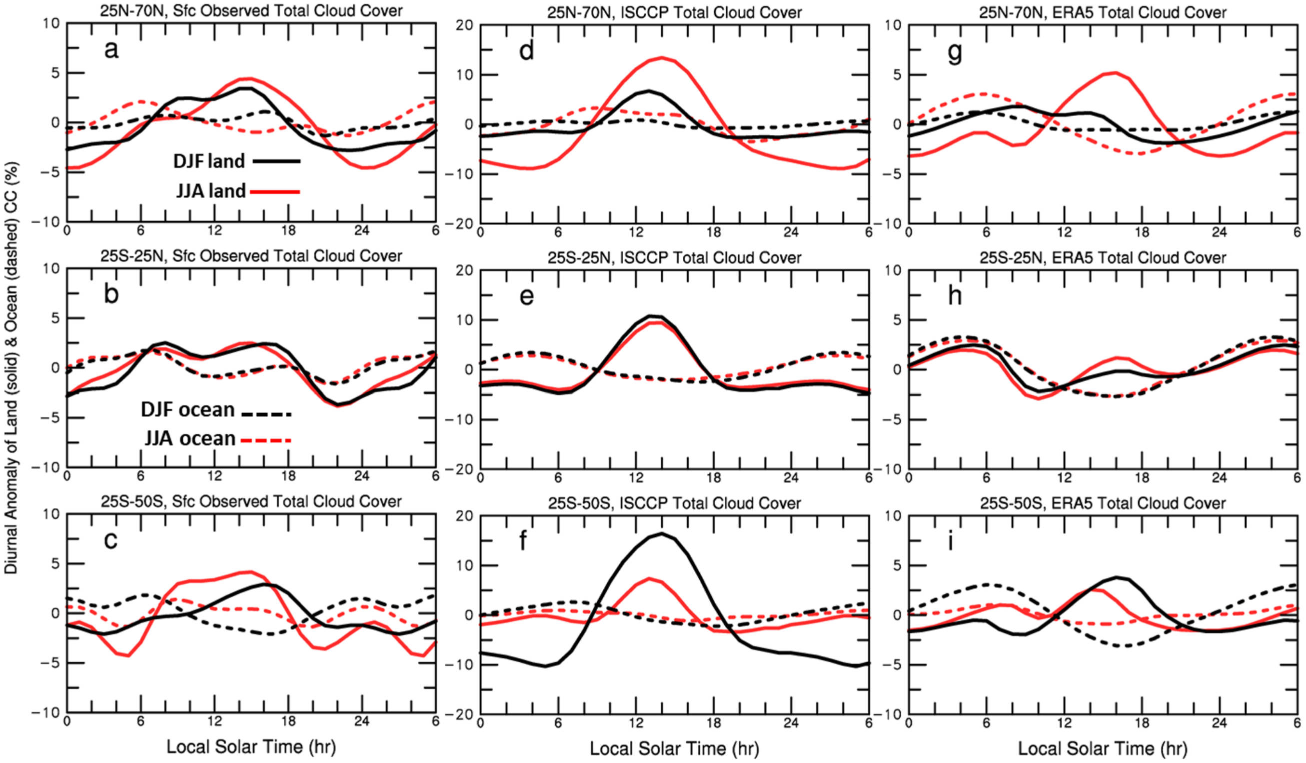

Fig. 12 Mean diurnal cycles of total cloud cover (in %) from **a**–**c** surface observations during 1976–2007 (excluding dark-night observations), **d**–**f** ISCCP H-series during 1983–2017, and **g**–**i** ERA5 during 1979–2020 averaged over land (solid lines) and ocean (dashed lines) in December–January–February (DJF, black lines) and June–July–August (JJA, red lines) within the **a**, **d**, **g** northern extra-tropics (25° N–70° N), **b**, **e**, **h** tropics (25° S–25° N), and **c**, **f**, **i** southern extra-tropics (25° S–50° S). The mean composite diurnal cycle was derived by first converting the UTC time into local solar time (LST = UTC + longitude/15, where longitude varies from − 180 to + 180, negative longitudes for the western hemisphere), and then averaging the diurnal anomalies (relative to the long-term mean of the daily mean) at each nearest LST hour over all the land or ocean grid boxes

DJF and 12–16 LST in JJA over land in both the surface and satellite observations; while the phase over the oceans is noisy with a tendency to peak around midnight-morning (Fig. 15g–j). ERA5 clouds show more coherent phase over the oceans, with a peak around 00–04 LST over most low-latitude oceans and 04–06 LST over extratropical oceans; over land, ERA5 JJA clouds peak in early to late afternoon over northern hemisphere land, where the peak is around 06–10 LST in DJF, which is much earlier than the observations (Fig. 15k, l).

The amplitude and phase of the 24-h harmonic in low clouds (Fig. 16) are comparable to those in total cloud cover in surface observations, suggesting that total cloud diurnal cycle mainly comes from low clouds. In ISCCP and ERA5, however, the phase of low cloud diurnal cycle differs substantially from that of total clouds: ISCCP low clouds tend to peak around 12-14LST over most land for both JJA and DJF, while ERA5 low clouds peak round 06–10 LST over land and many oceans (Fig. 16i–l), which is consistent with the zonal averages shown in Fig. 14. Given that surface observations are most reliable for low cloud cover, I believe that the results from surface observations in Fig. 16 are likely to be more reliable.

Besides cloud cover, cloud-base height also exhibits considerable diurnal variations (Fig. 17), with a minimum in the early afternoon and a maximum around midnight in surface observations over both land and ocean. The mean amplitude is about 150 m over warm-season land and only about 50 m over cold-season land and over the oceans. As the cloud base is visually estimated by trained observers, the amplitude likely contains substantial uncertainties. The daytime minimum cloud base is likely due to formation of low cumulus clouds from late morning to early afternoon; these cumulus clouds tend to dissipate after moist deep convection in the late afternoon or evening over warm-season land. ERA5 cloud base also shows considerable diurnal variations with an amplitude of ~ 200 m over warm-season land and slightly smaller over the oceans and cold-season land, a peak in the evening and a minimum in the morning between 06 and 12 LST (Fig. 17g–i). Thus, its amplitude is slightly stronger, and its phase is several hours earlier than the surface observations.

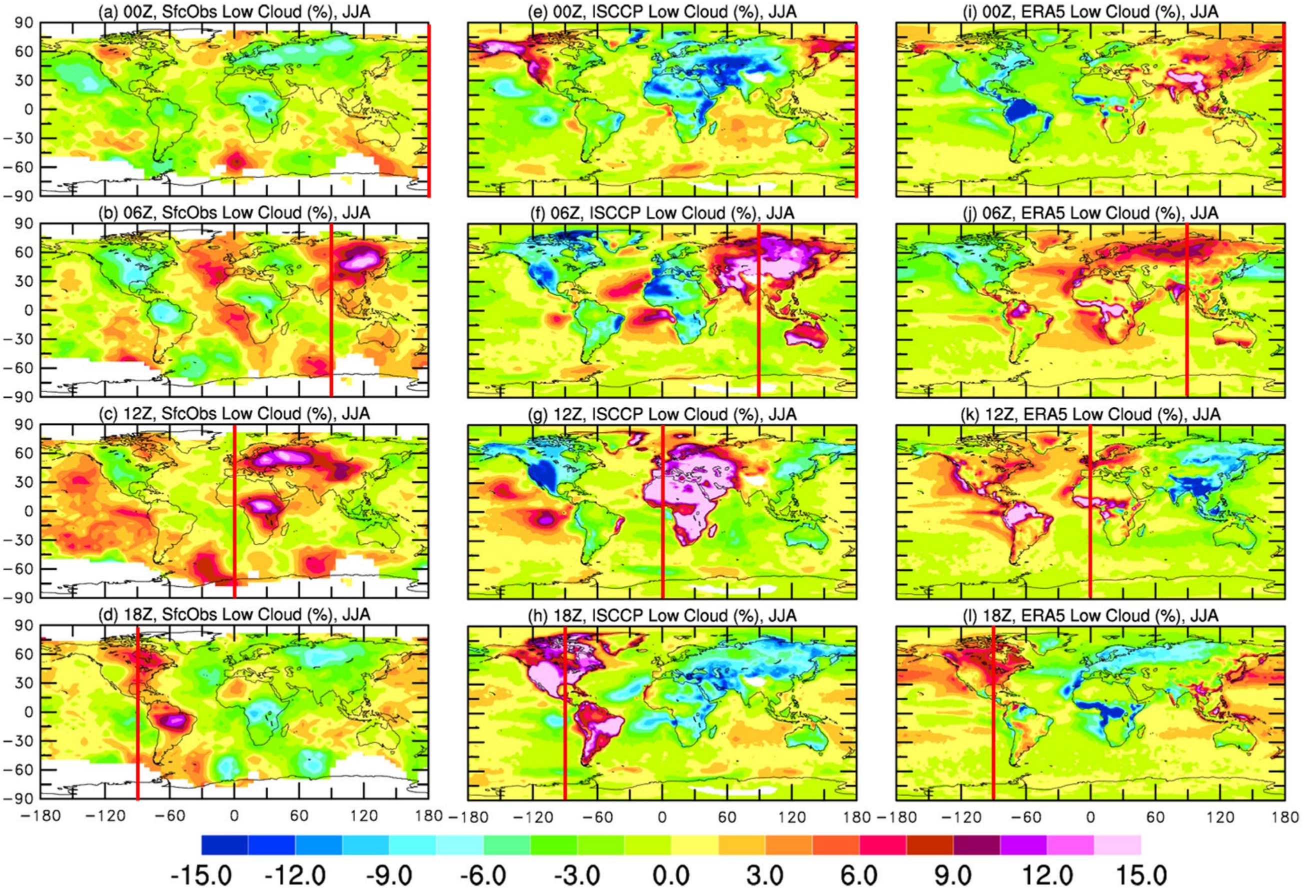

Fig. 13 Same as Fig. 11 but for low cloud cover, which is defined as the % of the sky covered by clouds with a base below 2 km above the ground for surface observations, and as the % of the grid-box area covered by clouds with a top below 680 hPa (~3.5 km) for ISCCP or by clouds occurring within the lower approximately 2 km for ERA5

3.3 Diurnal cycle in PBLH, CAPE and CIN in ERA5

ERA5 calculates PBLH based on assimilated radiosonde and other profile data and the commonly used bulk Richardson number method (Zhang et al. 2020). Therefore, ERA5 should provide a useful estimate of PBLH and its diurnal variations with hourly resolution. Figure 18 shows that land PBLH is typically around 250 m at night and increases after sunrise to a peak around 14–15 LST of about 1500–1900 m in the warm season and about 650–1100 m in the cold season. The results are comparable to previous estimates based on in-situ soundings and other measurements (Liu and Liang 2010; Gu et al. 2020; Zhang et al. 2020; Guo et al. 2021). Over the oceans, ERA5 PBLH diurnal variations are small and noticeable only in the tropics, where there is a minimum around 04 LST. PBLH estimates from soundings from sparse oceanic field campaigns (Liu and Liang 2010) and twice-daily operational soundings from coastal and island stations (Gu et al. 2020) show much higher PBLH around noontime than at night over many tropical and midlatitude oceans. This suggests that the lack of SST and marine air temperature diurnal cycles in ERA5 (Dai 2023) may have contributed to its weak PBLH diurnal cycle over oceans. Interestingly, marine PBLH is considerably higher in the cold season (around 1000 m) than in the warm season (~530 m over 25° N–70° N and 820 m over 25° S–50° S) in the extra-tropics. I was unable to find discussions on this seasonal difference in previous studies. One plausible explanation is that marine PBLH depends on the mixing strength induced by low-level winds, which are stronger in the cold season than in the warm season, rather than the mixing induced by surface heating as for continental PBLH. Over tropical oceans, JJA PBLH is slightly higher (by ~35 m) than that in DJF. This difference, together with the weak morning minimum and midday peak, may be partly due to the influence from tropical land, which has a higher daytime PBLH in JJA than DJF, although the nighttime PBLH over tropical land is very similar for both seasons. In the tropics, it is possible that the higher daytime marine PBLH in JJA resulting from strong continental influence may persist into the nighttime, leading to higher nighttime PBLH as well.

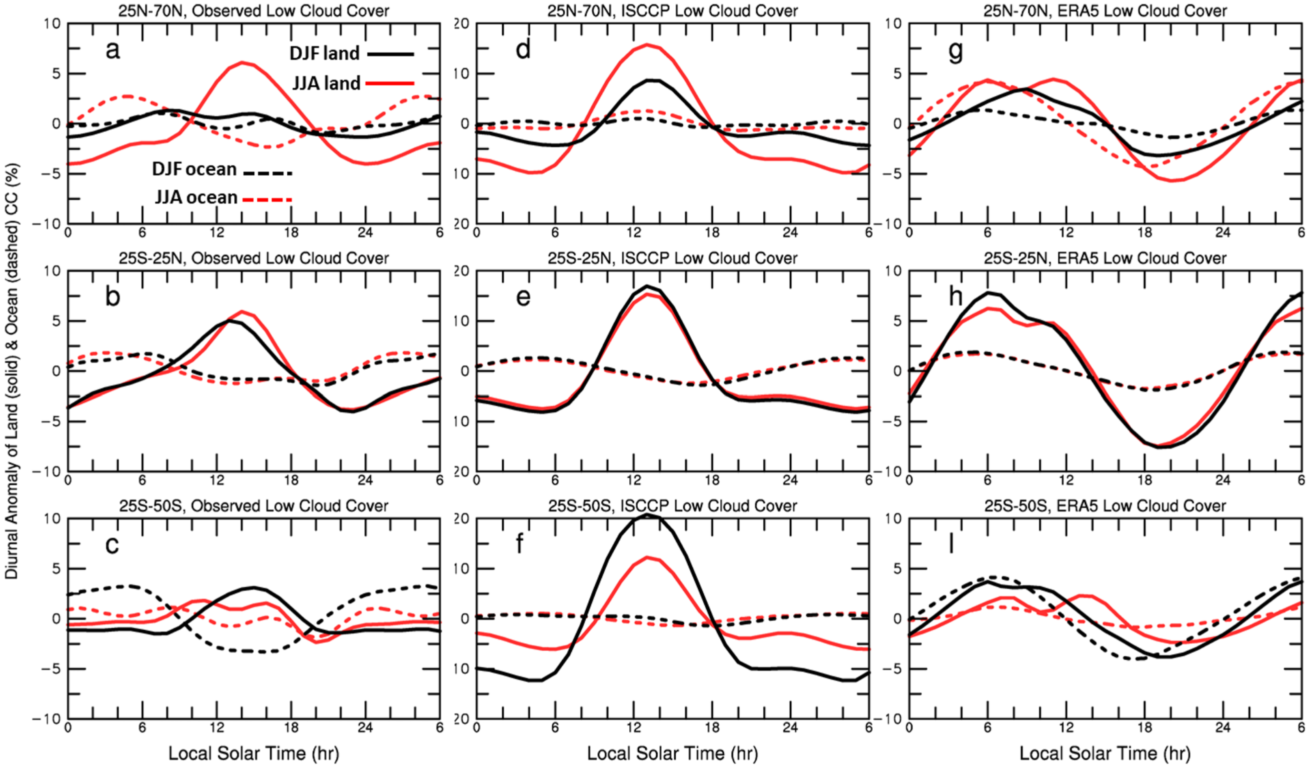

Fig. 14 Same as Fig. 12 but for low cloud cover

Figure 19 shows the amplitude and phase of the 24-h harmonic of the diurnal variations in the long-term mean PBLH from ERA5 for DJF and JJA. Clearly, the PBLH has the largest diurnal amplitude over inland areas during summer, especially drylands such northern Africa, the Middle East, the western North America, southern Africa, and Australia, where summer daytime solar radiation can quickly heat up the surface, leading to large sensible heat fluxes into the PBL, which increases the turbulent mixing and height of the PBL. The amplitude over these drylands can reach 1000–1500 m during summer. In DJF, the PBLH shows much weaker diurnal amplitudes of 50–400 m over the northern mid-high latitude land (Fig. 19a), while the amplitude is still large over most Southern Hemisphere land in JJA. Over most oceans, ERA5 PBLH shows small diurnal amplitudes (< 50 m) that are slightly larger over the tropical regions and the summer subtropical areas (Fig. 19a, b), which is likely linked to ERA5's use of daily-mean SST. The PBLH generally peaks around 13–15 LST over most land areas for both DJF and JJA (slightly earlier in JJA over many Northern Hemisphere lands); over most oceans, it peaks in late afternoon to evening (16–20 LST), although the peak is in the morning (08–12 LST) over some coastal areas, the northern North Pacific and the Southern Ocean (Fig. 19c, d).

CAPE (the positive buoyancy experienced by a listed parcel above the level of free convection, LFC), and CIN (the negative buoyancy a lifted parcel needs to overcome before reaching the LFC) are two metrics commonly used to quantify atmospheric thermodynamic conditions for convection (Chen et al. 2020; Chen and Dai 2023). Their diurnal variations are tightly linked to the diurnal cycle of moist convection and precipitation over warm-season land (Dai et al. 1999). Here, I compare the mean diurnal variations in ERA5 CAPE and CIN with those estimated from homogenized radiosonde temperature and humidity data, which are available only at 00 and 12 UTC from around 300–500 land stations mostly located in the Northern Hemisphere (Chen and Dai 2023). I averaged the 1979–2020 mean from all the stations within each of the three latitudinal bands to the nearest 3-hourly intervals (00, 03, 06, 09, 12, 15 and 21 LST). Given the twice daily soundings, the radiosonde data do not sample the diurnal cycle adequately. Nevertheless, they provide some qualitative check of the diurnal variations in ERA5 CAPE and CIN over land.

Figure 20 shows that ERA5 CAPE and CIN have considerable diurnal variations during the warm season over both land and ocean, and the CAPE's phase tends to be opposite over land and ocean, with near-noontime peak (minimum) and an early morning minimum (peak) over land (ocean). The day-night phase contrast for CAPE is consistent with the estimates from field experiments over the tropical Indian Ocean (Bellenger et al. 2010), India (Ratnam et al. 2013),

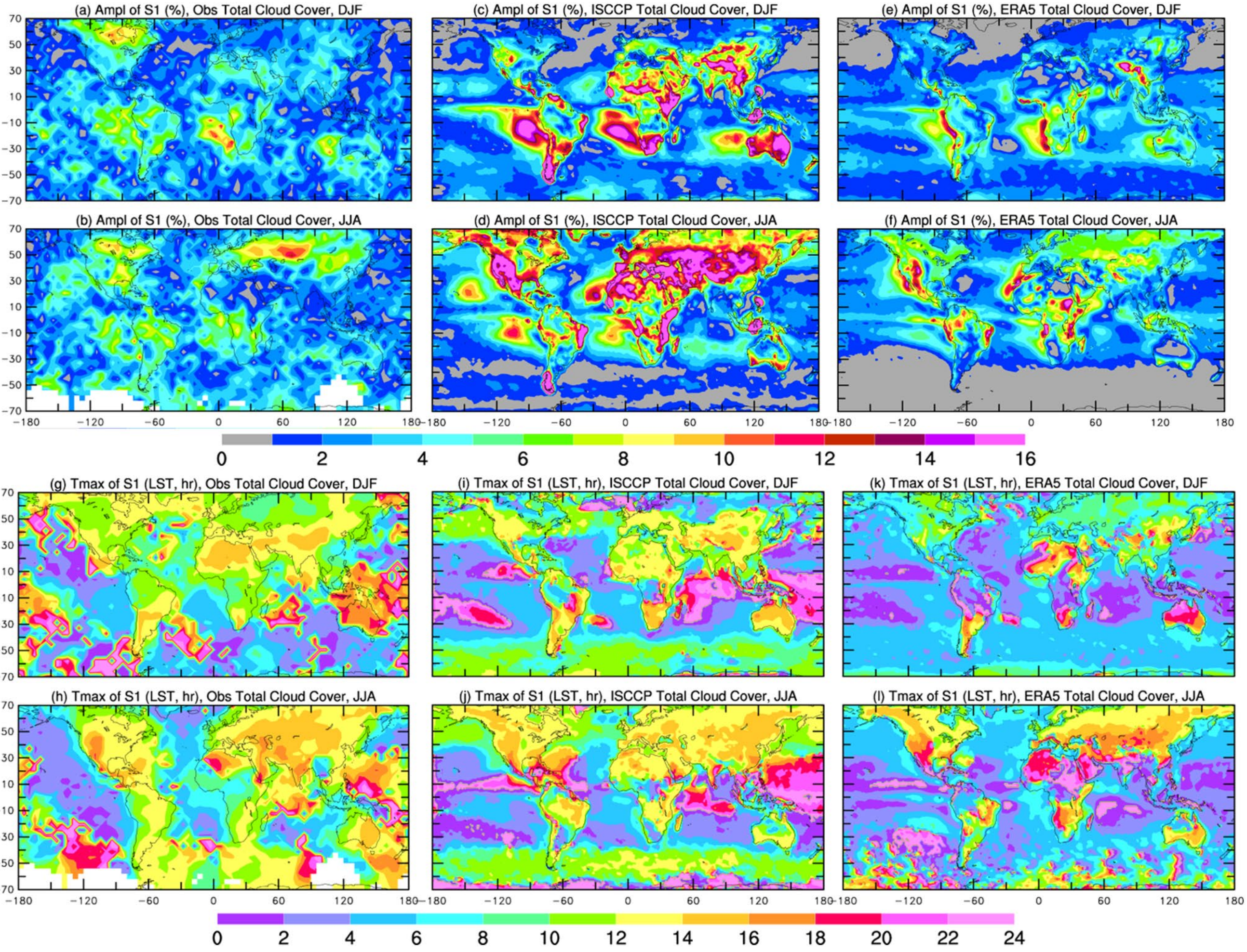

Fig. 15 **a**–**f** The amplitude (in % of the sky) of the 24-h harmonic of the mean diurnal variations in **a**, **c**, **e** DJF and **b**, **d**, **f** JJA total cloud cover from **a**, **b** surface observations, **c**, **d** ISCCP, and **e**, **f** ERA5. **g**–**l** Same as **a**–**f** but for the local solar time (LST, in hours) of the peak of the 24-h harmonic. See Fig. 10 for the data averaging periods. The long-term mean diurnal anomalies were fitted with the 12- and 24-h harmonics. The 12-h harmonic is much weaker than the 24 h harmonic

and the Amazon (Tang et al. 2016). While the near-noontime peak CAPE over land is likely due to solar heating and the resultant surface heat fluxes, the cause of the early morning maximum CAPE over ocean, which could contribute to the early morning peak in precipitation over ocean (Figs. 4 and 7), requires investigation. Possible causes may include radiative cooling of the free troposphere and oceanic heating of the surface air at night. In general, CIN's diurnal cycle is nearly out of phase with CAPE, with an early afternoon minimum and elevated values at night over land, and a late afternoon peak (around 16–18 LST) and morning minimum (around 04–06 LST) over ocean (Fig. 20d–f). The CIN's oceanic diurnal phase is consistent with the observed CIN under conditions without large SST diurnal variations over the tropical Indian Ocean (Bellenger et al. 2010). In the tropics, the CAPE and CIN diurnal variations are large and similar for DJF and JJA, while in the extratropics, the cold-season diurnal variations are weak, especially for CAPE. The diurnal amplitude over ocean is only about one fifth of that over land (note the different y-axis scales on Fig. 20) for both CAPE and CIN, which is not surprising given the strong surface heating over land during the day. Warm-season ERA5 CAPE over land shows a small but robust dip around 16 LST in all latitudinal zones, which is likely related to the peak precipitation around 15–16 LST (Figs. 4g–i and 5d–f), as moist convection consumes CAPE in the atmosphere. The CIN variations estimated using the sounding data over land are generally consistent with ERA5 CIN (Fig. 20d–f), confirming the daytime minimum and nighttime maximum over land, which are expected given the reduced stability during the day due to solar heating and increased stability at night. However, the sounding-based CAPE variations are noisy and do not always agree with the ERA5 CAPE variations

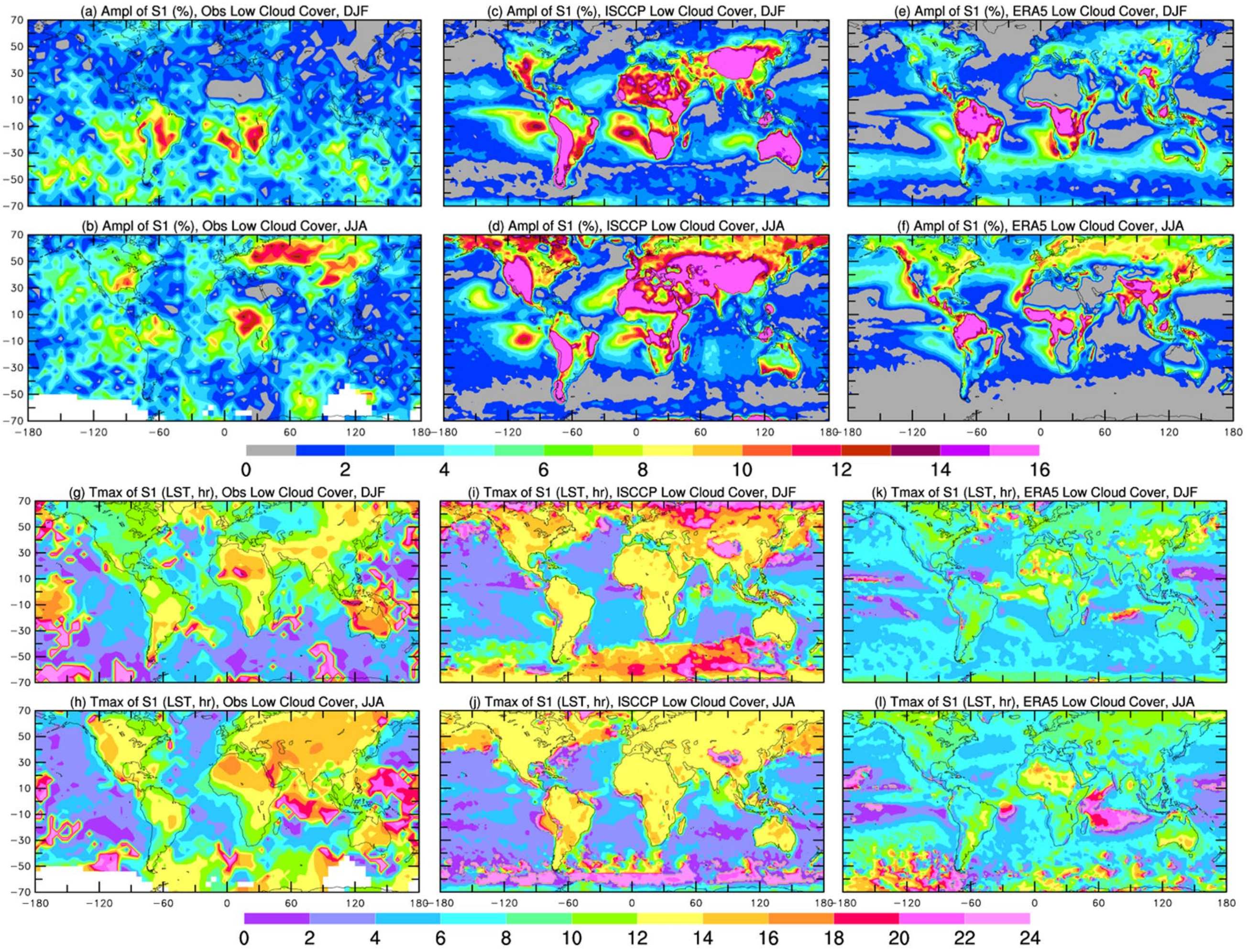

Fig. 16 Same as Fig. 15 but for low cloud cover

(Fig. 20a–c). This may be partly due to insufficient temporal sampling by the twice-daily soundings.

Amplitude maps of the diurnal (24-h) harmonic of the ERA5 CAPE and CIN (not shown) revealed that CAPE diurnal variations are largest over tropical land areas, such as tropical South America, Africa and the Maritime Continent around Indonesia, while CIN shows strongest diurnal variations over many drylands, such as the western U.S. and northern Africa in JJA.

3.4 Diurnal cycle in surface energy fluxes

The strong diurnal cycle over land relative to ocean in surface air temperature and pressure (Dai 2023), precipitation, PBLH, CAPE and CIN results mainly from strong daytime heating from the land surface, which absorbs solar radiation and heats up more quickly than the ocean surface due to the low heat capacity and slow downward transfer of heat in land surface layer. Therefore, we need to examine diurnal variations in surface energy fluxes in order to understand the diurnal cycle in many other fields. Here I examine the zonally-averaged mean diurnal cycles in surface shortwave (SW) and longwave (LW) radiation, and sensible heat (SH) and latent heat (LH) fluxes from ERA5 and from CERES satellite-based estimates (available only for SW and LW).

Figure 21 shows that daytime surface net SW radiation (SWnet), which depends on atmospheric (mainly cloud) and surface albedo, is higher over ocean than over land in both the tropics and northern extratropics, but the opposite over the southern extratropics, where the land areas have fewer clouds (Fig. 10). Over tropical oceans, the mean SWnet noon peak can reach 750 W m^{-2} in DJF and around 700 W m^{-2} in JJA, while the noon peak is around 600 W m^{-2} for both DJF and JJA over tropical land (Fig. 21a–c). ERA5 captures the SWnet magnitude and its diurnal variations seen in CERES remarkably well, including the seasonal and land–ocean differences. This may be partly due to ERA5's

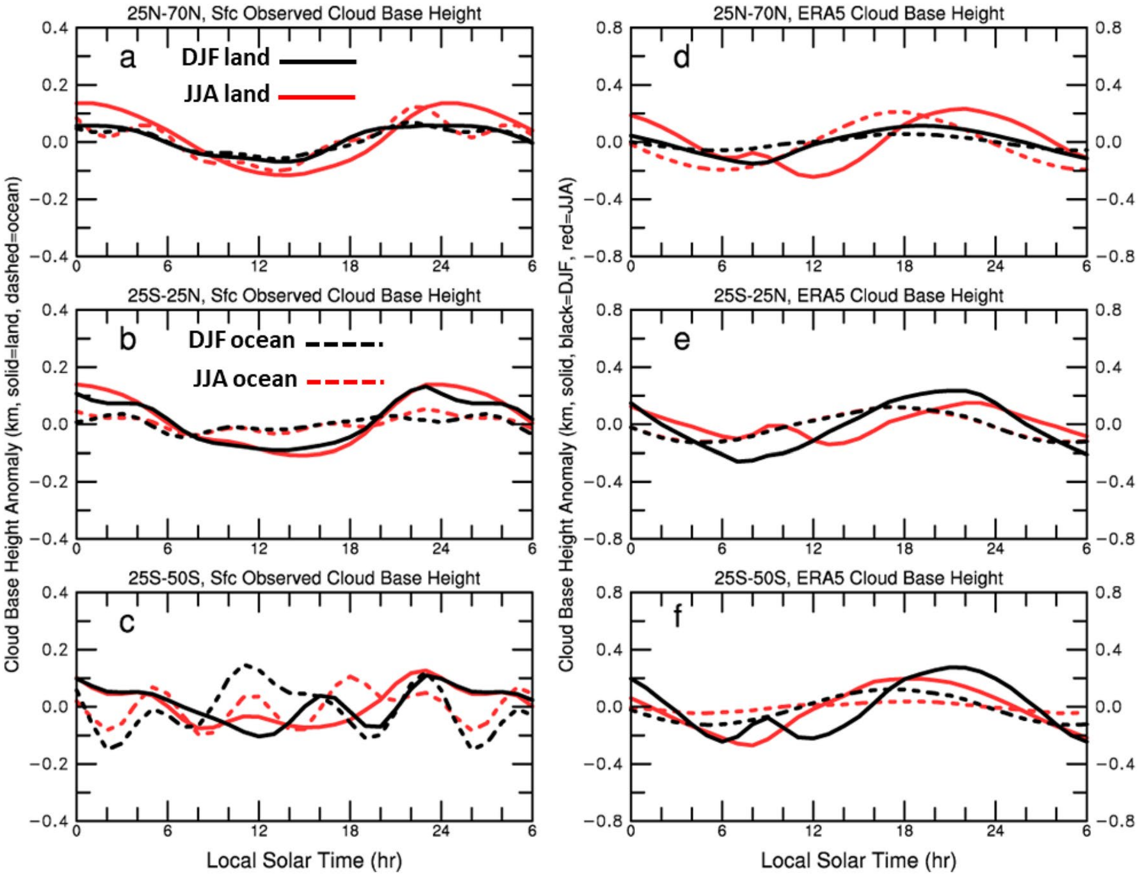

Fig. 17 Mean diurnal cycles of cloud base height (in km above the ground) from **a**–**c** surface observations during 1976–2007 (excluding dark-night observations) and **d**–**f** ERA5 during 1979–2020 averaged over land (solid lines) and ocean (dashed lines) in December–January–February (DJF, black lines) and June–July–August (JJA, red lines) within the **a**, **d** northern extra-tropics (25° N–70° N), **b**, **e** tropics (25° S–25° N), and **c**, **f** southern extra-tropics (25° S–50° S). The mean composite diurnal cycle was derived by first converting the UTC time into local solar time (LST = UTC + longitude/15, where longitude varies from − 180 to + 180, negative longitudes for the western hemisphere), and then averaging the diurnal anomalies (relative to the long-term mean of the daily mean) at each nearest LST hour over all the land or ocean grid boxes

realistic simulations of cloud cover (Fig. 10), which has a major impact on surface SW radiation.

Diurnal variations in surface net LW radiation (LWnet) from CERES and ERA5 are also very similar, both showing a peak of 100–150 W m^{-2} around noon over extratropical land and around 13 LST over tropical land (Fig. 22). The near-noontime peak in LWnet results mainly from the strong peak in surface upward LW radiation around 13 LST, while the peak in surface downward LW radiation (also around 13 LST) is comparatively weak (figure omitted). Nighttime LWnet is around 45–55 W m^{-2} and upward over both land and ocean in the tropics for both DJF and JJA, and slightly higher (lower) during the warm season over land (ocean) in the extratropics. LWnet and surface upward LW radiation (figure omitted) over ocean shows little diurnal variation for both ERA5 and CERES, which used atmospheric profiles from NASA's reanalysis product that also did not include SST diurnal variations. CERES's surface downward LW radiation over ocean shows small diurnal variations (figure omitted), which contribute to the small diurnal variations in its LWnet over ocean (Fig. 22a–c).

The near-noontime peak in LWnet over land indicates that the surface-air temperature gradient peaks near the noon, which is confirmed by the noontime peak in surface SH flux from ERA5 over land (Fig. 23). The noontime peak can reach 195 W m^{-2} over tropical land and 260 W m^{-2} over southern extratropical land in DJF (Fig. 23). Surface LH flux over land also shows a sharp peak slightly after 12 LST, with a mean amplitude comparable to that for SH fluxes (Fig. 23d–f). Such a noontime peak is consistent with bulk formula-based estimates over the central U.S. (Zhang and Klein 2010) but is a few hours earlier than that observed for SH fluxes over the Tibetan Plateau (Zhu et al. 2023). Oceanic SH and LH fluxes show little diurnal variations in ERA5, in contrast to estimates based on tropical buoy

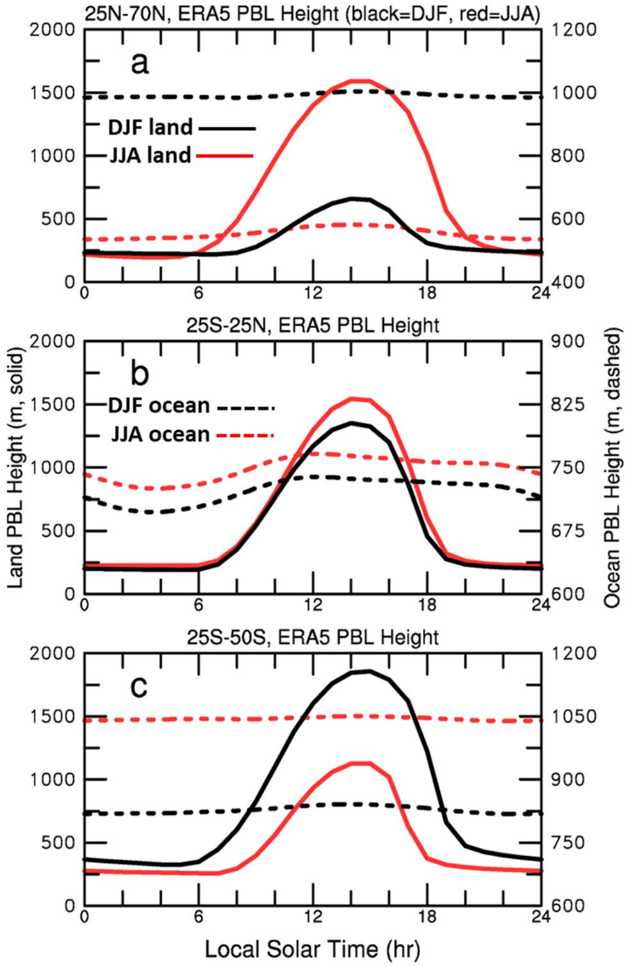

Fig. 18 Same as Fig. 17 but for the zonal-mean diurnal variations in the planetary boundary layer height (m above the surface) averaged over 1979–2020 from ERA5. Note the daily mean is included in the plot and ocean PBL height is plotted on the right y-axis

observations which show a noon-early afternoon peak for LH fluxes (Yan et al. 2021). Satellite-based LH estimates also show considerable diurnal variations over the oceans, especially over the western boundary currents and coastal regions (Clayson and Edson 2019). The SH flux is low (~ 10 W m^{-2}) over tropical oceans, while it is slightly higher (~ 35 to 40 Wm^{-2}) over the extratropical oceans during the cold season when the ocean-air temperature gradient is larger and it is windy. In contrast, the LH flux is comparatively high over the oceans, around 140 and 50–115 W m^{-2} respectively over the tropical and extratropical oceans, where the LH flux is also higher in the cold season. Maps of the S1 amplitude (figure omitted) for SH fluxes revealed that the largest SH diurnal variations are over drylands during the warm season, such as Southwest North America, northern Africa and the Middle East and northern Australia in JJA and the central and southern Australia, southern African, and southern Argentina in DJF, where the amplitude can reach 120–180 W m^{-2}. In contrast, the largest diurnal amplitude for LH fluxes is seen over the warm-season wet land areas, such as tropical South America and Africa in DJF, and Central America, northern South America, northern Central Africa, Southeast Asia, and the central-eastern U.S. in JJA; whereas the mean LH flux and its diurnal variations over drylands are small as expected.

4 Summary and discussion

In this study, I have examined the mean diurnal variations over the globe in precipitation, cloud cover and cloud base height, PBLH, CAPE, CIN, and surface fluxes in ERA5 and compared them with available observations. Table 1 summarizes the key findings. ERA5 captures the seasonal climatology of precipitation and cloud cover remarkably well, especially given that ERA5 does not assimilate their observations over most of the globe. Surface and satellite observations show that warm-season precipitation exhibits a robust diurnal cycle, with an amplitude of ~ 20 to 50% of the daily mean and a peak around 14–18 LST over most land areas and 04–08 LST over most oceans in surface observations, consistent with previous estimates (e.g., Dai 2001a; Dai et al. 2007). ERA5 approximately captures these features with a slightly earlier peak (by ~ 2 h) over both land and ocean and a stronger amplitude over land. These biases mainly come from convective precipitation in ERA5, as the non-convective or large-scale precipitation shows a weak diurnal cycle with a morning (06–10 LST) peak over many land and ocean areas. On the other hand, warm-season precipitation from IMERG satellite product captures mainly the diurnal cycle of convective precipitation with a peak around 16–20 LST, as noticed previously (Dai et al. 2007). Despite the lack of SST diurnal variations and resultant weak marine surface diurnal cycle in ERA5 (Dai 2023), ERA5 oceanic precipitation shows robust diurnal variations that are comparable to surface and satellite observations. This suggests that oceanic precipitation diurnal cycle is likely controlled by free-tropospheric processes such as large-scale land–ocean diurnal circulation and local radiative cooling (Gray and Jacobson 1977; Dai 2001a), rather than near-surface diurnal variations in contrast to land precipitation diurnal cycle, which is strongly influenced by daytime surface heating induced by solar radiation (Dai et al. 1999; Liang et al. 2004).

Surface and satellite observations show that there are more clouds during daytime (nighttime) over land (ocean), as noticed previously (Hahn et al. 1995). This day-night cloudiness difference is qualitative consistent with the different diurnal phase of precipitation over land and ocean. Surface observations show a peak around 14 LST for warm-season clouds and elevated cloudiness around 08–16 LST for the cold season over extratropical land. Cloud cover over

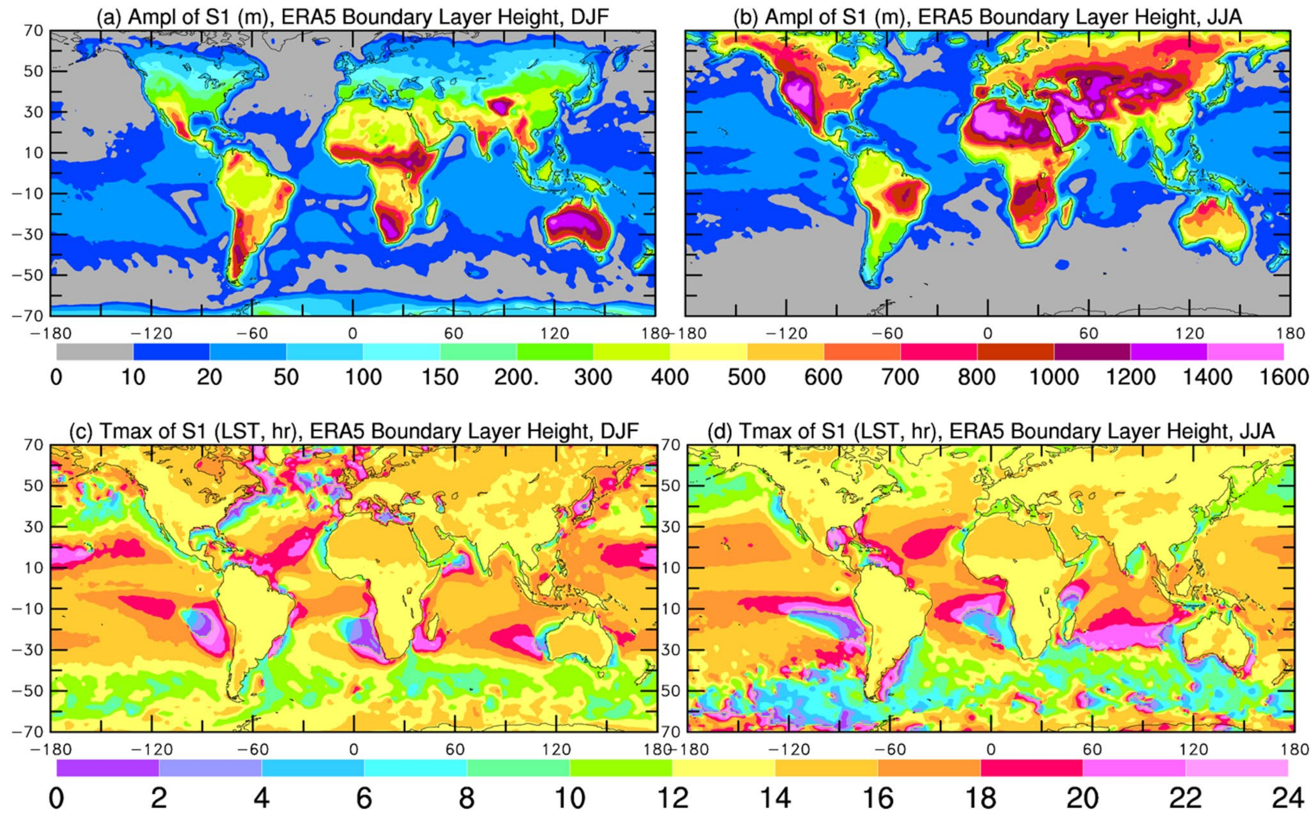

Fig. 19 **a**, **b** The amplitude (in m) of the 24-h harmonic of the mean diurnal variations in **a** DJF and **b** JJA planetary boundary layer height (PBLH) from ERA5 averaged over 1979–2020. **c**, **d** Same as **a**, **b** but for the local solar time (LST, in hours) of the peak of the 24-h harmonic. The long-term mean diurnal anomalies for each hour were fitted with the 12- and 24-h harmonics. The 12-h harmonic is much weaker than the 24 h harmonic (cf. Figs. 1 and 18)

tropical land shows two weak peaks around 07 and 16 LST. Marine cloudiness diurnal variations are small, with slightly more clouds during early morning. The ISSCP satellite data show sharper early afternoon peaks in cloud cover over land for both JJA and DJF than in surface observations, while its marine clouds also show small diurnal variations with slightly more clouds at night. In general, ERA5 cloud diurnal anomalies are more comparable to surface observations than to ISCCP, which has too strong diurnal variations over land partly due to the excessive diurnal variations in its low clouds, whose observations are less reliable by satellites. In surface and satellite observations, low clouds show diurnal variations similar to those in total clouds and thus contribute the most to the diurnal variations in total cloud cover, as middle and high clouds exhibit only small diurnal variations. However, ERA5 low clouds exhibit a different phase (peak around 06–08 LST for both DJF and JJA) compared to that in its total clouds (peak around 14–18 LST over warm-season land). Even though the definitions of low clouds may differ somewhat among these datasets (Fig. 13), such a large phase difference in ERA5 low clouds is still a concern.

Surface visual observations of cloud base height show an early afternoon minimum (likely due to late morning formation of cumulus clouds) and a midnight maximum over both land and ocean, with a mean amplitude of about 150 m over warm-season land and only about 50 m over cold-season land and over the oceans. ERA5 cloud base shows a slightly stronger diurnal cycle, with an amplitude of ~ 200 m over warm-season land and slightly smaller over the oceans and cold-season land, and an earlier peak in the evening and a minimum in the morning between 06 and 12 LST.

ERA5, which assimilates sounding profile data, shows that land PBLH is typically around 250 m at night but increases rapidly after sunrise to a peak around 14–15 LST of about 1500–1900 m in the warm season and about 650–1100 m in the cold season, consistent with previous estimates based on limited sounding data (Liu and Liang 2010; Gu et al. 2020; Zhang et al. 2020; Guo et al. 2021). The strongest PBLH diurnal cycle is seen over summer drylands, where the diurnal amplitude can reach 1000–1500 m with a peak around 13–15 LST due to strong sensible heating from the ground. Likely influenced by the use of daily mean SST in ERA5, marine PBLH in ERA5 exhibits small diurnal

Fig. 20 Same as Fig. 17 but for the zonal-mean diurnal variations in the **a**–**c** CAPE and **d**–**f** CIN (expressed in positive values) averaged over 1979–2020 from ERA5. The dot (crosses) are the estimates for JJA (DJF) based on twice daily radiosonde observations over land during 1979–2020 (requiring 20 or more years of data) from Chen and Dai (2023), with CAPE values (based on a reversible process) multiplied by 0.5 in order to use the same y axis in **a**–**c**

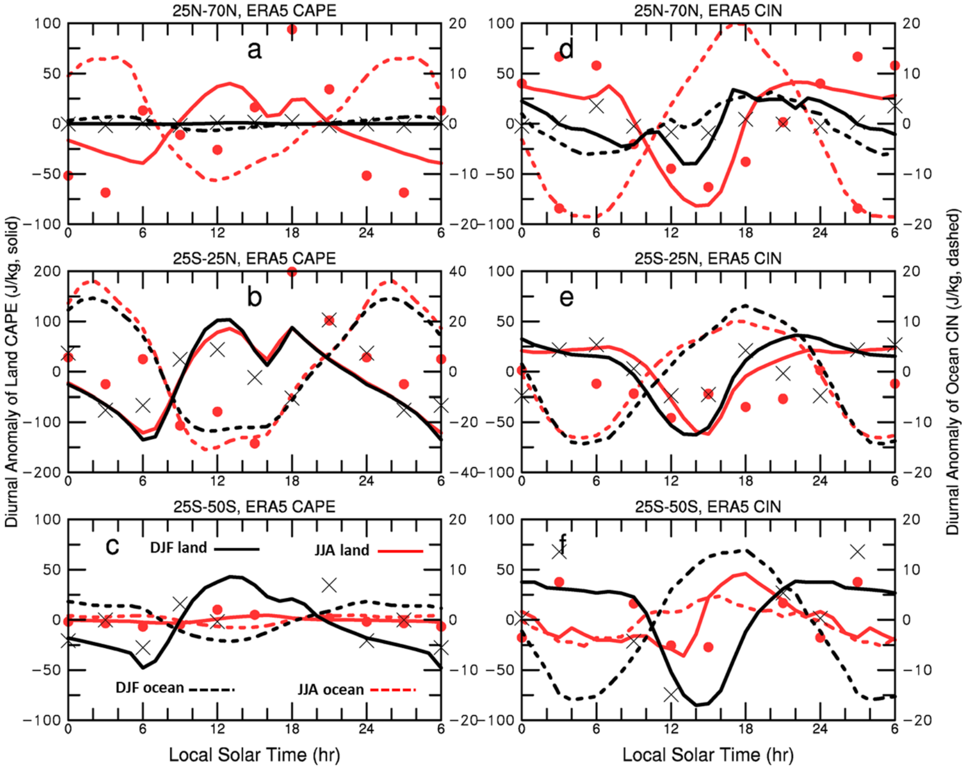

Fig. 21 Long-term mean diurnal cycles of surface net shortwave (SW) radiation (in W m^{-2}, positive downward) from **a**–**c** CERES satellite product during 2000–2022 and **d**–**f** ERA5 during 1979–2020 averaged over land (solid lines) and ocean (dashed lines) in December–January–February (DJF, black lines) and June–July–August (JJA, red lines) within the **a**, **d** northern extra-tropics (25° N–70° N), **b**, **e** tropics (25° S–25° N), and **c**, **f** southern extra-tropics (25° S–50° S). The mean composite diurnal cycle was derived by first converting the UTC time into local solar time (LST = UTC + longitude/15, where longitude varies from − 180 to + 180, negative longitudes for the western hemisphere), and then averaging the flux values at each nearest LST hour over all the land or ocean grid boxes within the latitudinal zone

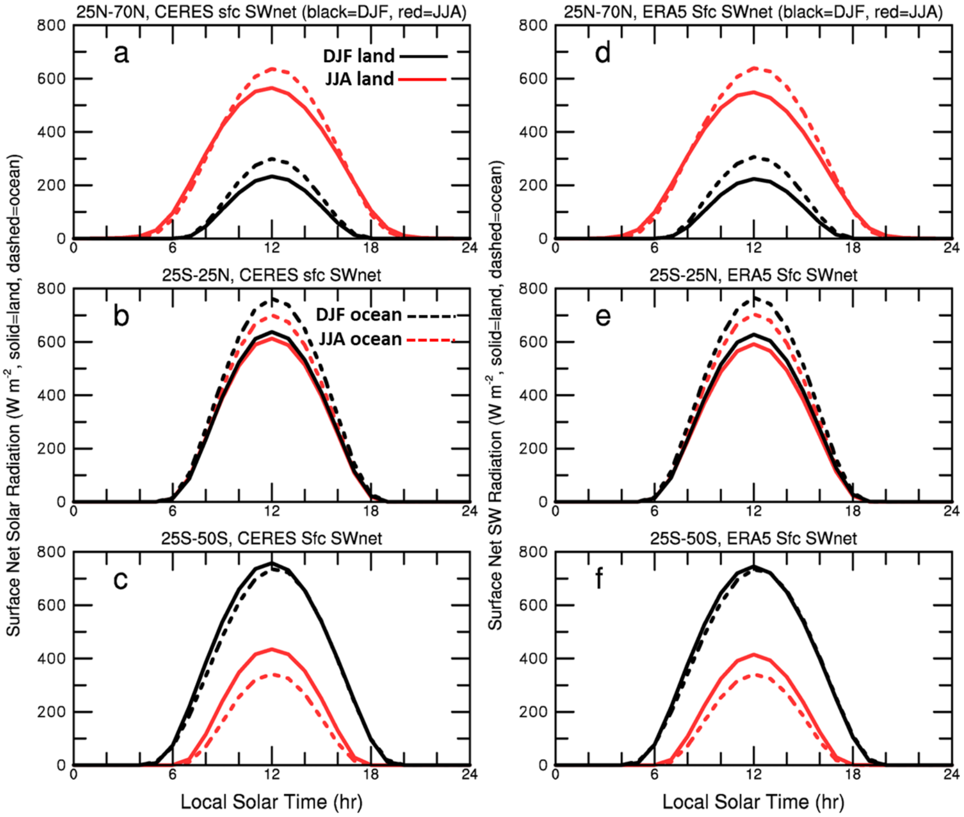

Fig. 22 Same as Fig. 21, but for surface net longwave radiation (in W m^{-2}, positive upward)

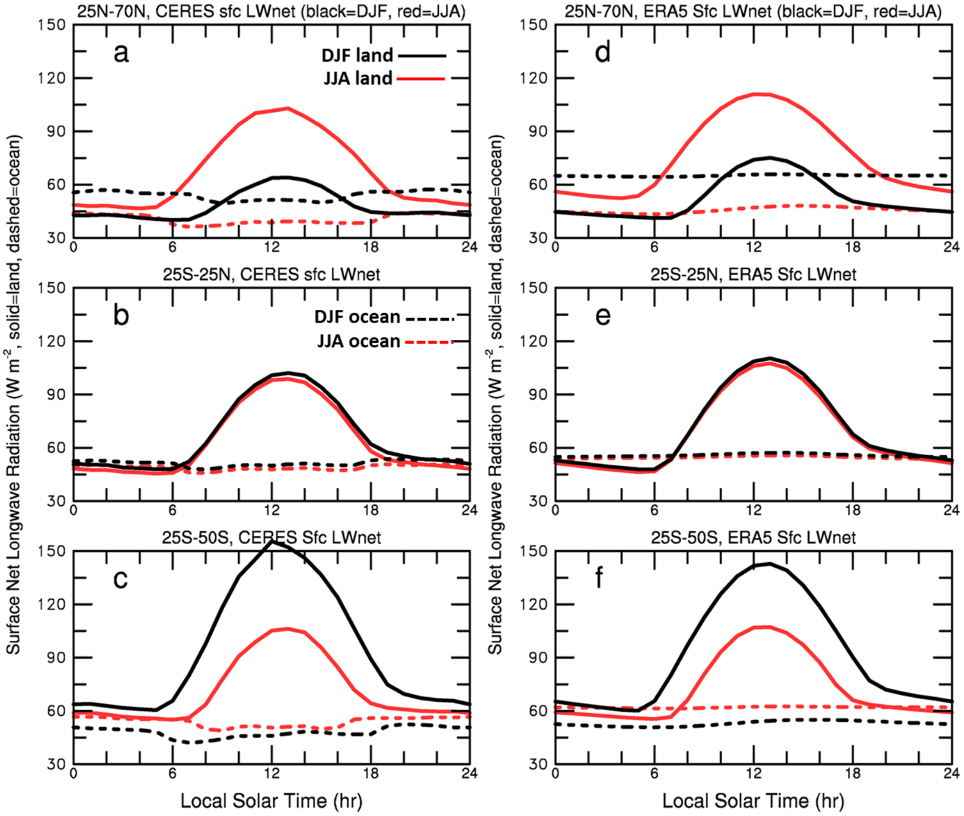

Fig. 23 Same as Fig. 21, but for surface sensible heat (SH) (left) and latent heat (LH) fluxes (in W m^{-2}, positive upward) from ERA5

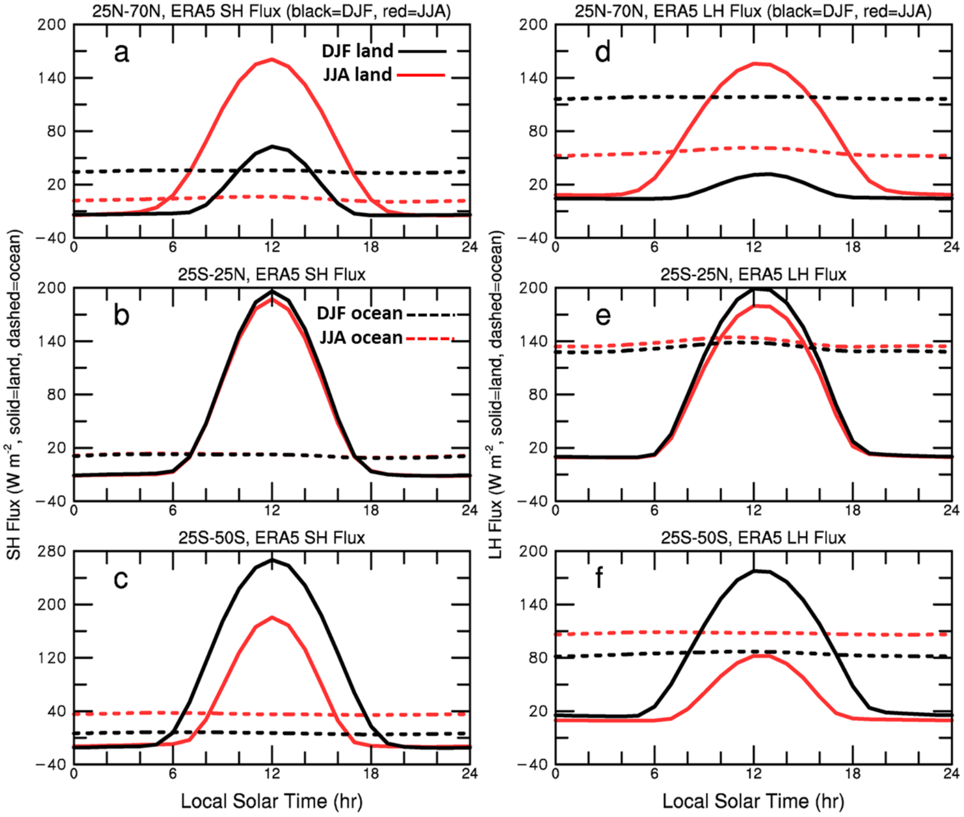

Table 1 A summary of the observed diurnal features and ERA5's performance

Variable	Observations	ERA5 performance
Precipitation	Warm-season precipitation has a diurnal amplitude of ~ 20 to 50% of the daily mean, and a peak around 14–18 LST over most land areas and 04–08 LST over most oceans. IMERG captures mainly the diurnal cycle of convective precipitation with a peak around 16–20 LST.	Realistic seasonal precipitation distributions, slightly earlier (by 2 h) diurnal peak over both land and ocean and a stronger diurnal amplitude over land for warm-season precipitation, mainly due to diurnal biases in ERA5's convective precipitation. Robust diurnal cycle in oceanic precipitation despite its weak marine surface diurnal cycle due to ERA5's use of daily mean SST.
Clouds	There are more clouds during daytime (nighttime) over land (ocean), consistent with the precipitation diurnal phase over land and ocean. Warm-season clouds peak around 14 LST while cold-season cloudiness is elevated from 08 to 16 LST over extratropical land. Tropical land cloudiness peaks around 07 and 16 LST. Cloud diurnal variations are small over most oceans. ISCCP has too strong diurnal variations over land due to its excessive low-cloud variations. Cloud base height shows an early afternoon minimum and a midnight maximum over both land and ocean.	Realistic seasonal cloudiness distributions, large cloud amounts (mainly from low clouds) over the Southern Ocean and the central Arctic, where surface and satellite observations are less reliable. ERA5 total cloud diurnal anomalies are comparable to surface observations; however, unlike observations where low clouds dominate cloud diurnal variations, ERA5 low clouds show unrealistic diurnal phases (peak around 06–08 LST for both land and ocean). ERA5 cloud base shows a slightly stronger diurnal cycle, with an amplitude of ~ 200 m over warm-season land and slightly smaller over the oceans and cold-season land, and an earlier peak in the evening and a minimum between 06–12 LST.
PBLH		Land PBLH is around 250 m at night, increases after sunrise to a peak around 14–15 LST of about 1500–1900 m in the warm season and about 650–1100 m in the cold season, consistent with previous sounding-based estimates. Influenced by using daily mean SST, marine PBLH in ERA5 exhibits small diurnal variations (amplitude < 50 m) only in the tropics, inconsistent with previous estimates. Marine PBLH is higher in the cold season than in the warm season in the extratropics, implying that marine PBLH depends on low-level wind-induced mixing rather than surface heating
CAPE & CIN		ERA5 CAPE shows out-of-phase diurnal variations over land and ocean, with near-noontime peak (minimum) and an early morning minimum (peak) over land (ocean), consistent with limited observational results. CIN is roughly out-of-phase with CAPE The diurnal amplitude in marine CAPE and CIN is only ~ 1/5 of that over land
Surface fluxes	CERES satellite data show a noon peak of 750 W m^{-2} in DJF and 700 W m^{-2} in JJA for surface net shortwave radiation (SWnet) over tropical oceans, while the noon peak is ~ 600 W m^{-2} for both DJF and JJA over tropical land. Summer SWnet peak over the extratropics is comparable to the tropical peak, but lower in winter. Surface net LW radiation (LWnet) shows a peak of 100–150 W m^{-2} around noon over extratropical land and around 13 LST over tropical land; marine LWnet has little diurnal variation.	ERA5 captures well the diurnal cycles and their land–ocean and DJF-JJA differences in SWnet and LWnet seen in CERES satellite data. Both LWnet and land SH flux peak near noontime, and land LH flux peaks slightly after noon. The SH and LH phases are consistent with observations from limited locations. Marine SH and LH fluxes show little diurnal variation in ERA5, inconsistent with buoy and satellite data, likely related to ERA5's use of daily mean SST.

variations (amplitude < 50 m) that are noticeable only in the tropics, where there is a minimum around 04 LST, in contrast to previous estimates based on limited sounding data that show a robust noontime peak over many tropical and midlatitude oceans (Liu and Liang 2010; Gu et al. 2020). Marine PBLH is higher in the cold season (~ 1000 m) than in the warm season in the extratropics (~ 530 m over 25° N–70° N and 820 m over 25° S–50° S). This seems to imply that marine PBLH depends on low-level wind-induced mixing rather than surface heating.

ERA5 CAPE shows out-of-phase diurnal variations over land and ocean, with near-noontime peak (minimum) and an early morning minimum (peak) over land (ocean), consistent with limited observational results (Bellenger et al. 2010; Ratnam et al. 2013; Tang et al. 2016). The exact cause of the early morning maximum CAPE over ocean, which could contribute to the early morning peak precipitation over ocean, is unknown. One plausible explanation is the radiative cooling (Gray and Jacobson 1977) in the free troposphere coupled with a warm ocean surface (which keeps the near-surface air warm) at night, which could increase the instability of the atmosphere. CIN's diurnal cycle is approximately out of phase with CAPE, with an early afternoon minimum and elevated values at night over land, and a late afternoon peak (~ 16 to 18 LST) and morning minimum (~ 04 to 06 LST) over ocean, which is consistent with observed CIN over the tropical Indian Ocean (Bellenger et al. 2010). In the tropics, the CAPE and CIN diurnal variations are large and similar for DJF and JJA, while in the extratropics, their cold-season diurnal variations are small. The diurnal amplitude in marine CAPE and CIN is only about one fifth of that over land. CIN estimates based on homogenized station sounding data are generally consistent with ERA5 CIN, confirming the daytime minimum and nighttime maximum over land. However, the sounding-based CAPE variations are noisy and do not always agree with ERA5 CAPE, which may be partly due to limited temporal sampling by the twice-daily soundings.

ERA5 captures well the diurnal cycles and their land–ocean and DJF-JJA differences in surface net shortwave (SWnet) and longwave (LWnet) radiation seen in CERES satellite-based estimates. SWnet is higher over ocean than land over the tropics and northern extratropics (25° N–70° N) but is the opposite over the southern extratropics (25° S–50° S). Over tropical oceans, the mean SWnet noontime peak can reach 750 W m^{-2} in DJF and 700 W m^{-2} in JJA, while the noontime peak is ~ 600 W m^{-2} for both DJF and JJA over tropical land. LWnet from both CERES and ERA5 shows a peak of 100–150 W m^{-2} around noon over extratropical land and around 13 LST over tropical land. The near-noontime peak in land LWnet results mainly from the strong peak in surface upward LW radiation around 13 LST. Nighttime LWnet is around 45–55 W m^{-2} and upward over both land and ocean in the tropics for both DJF and JJA, and slightly higher (lower) during the warm season over land (ocean) in the extratropics. Marine LWnet shows little diurnal variation in both ERA5 and CERES, which may be partly due to their use of daily-mean SST.

The near-noontime peak in land LWnet is consistent with the noontime peak in ERA5 surface SH flux over land. The SH noon peak can reach 195 W m^{-2} over tropical land and 260 W m^{-2} over southern extratropical land in DJF. The largest diurnal amplitude of SH is seen over warm-season drylands, where the PBLH has the largest diurnal variations. Surface LH flux over land in ERA5 also shows a large peak (comparable to that of SH) slightly after 12 LST. These land SH and LH diurnal variations are broadly consistent with observational estimates from limited locations (Zhang and Klein 2010), although LH fluxes were shown to peak around 1500 LST over the Tibetan Plateau (Zhu et al. 2023). Marine SH and LH fluxes show little diurnal variation in ERA5, inconsistent with buoy-based estimates over tropical oceans (Yan et al. 2021) and satellite-based estimates of oceanic LH fluxes (Clayson and Edson 2019). This deficiency may partly result from ERA5's use of daily mean SST.

In summary (Table 1), I found that ERA5 does a remarkable job in capturing the observed seasonal climatology of precipitation and cloud cover and their diurnal variations, as well as the diurnal variations in surface energy fluxes, despite its deficiency in using daily-mean SST. Examinations of the seasonal and spatial patterns of the diurnal variations in precipitation, clouds, PBLH and other fields can help reveal the underlying controlling mechanisms. For example, the fact that ERA5 ocean precipitation shows a comparatively strong diurnal cycle despite its dampened near-surface diurnal variations due to its use of daily-mean SST (Dai 2023) suggests that oceanic precipitation diurnal cycle is likely controlled by free tropospheric processes, rather than near-surface diurnal variations, which are critical for continental precipitation diurnal cycle. Another example is that the much higher PBLH in the cold season than in the warm season over extratropical ocean suggests that low-level wind-induced mixing is the controlling factor for marine PBLH, in contrast to land PBLH that is controlled by turbulence mixing induced by daytime surface heating. The physical causes of many of the diurnal variations still require further investigation; for example, it is unclear why CAPE peaks in the early morning over ocean in ERA5. Is it linked to radiative cooling of the free troposphere and oceanic heating of the lower troposphere at night? The connection or relationship between the diurnal cycles in different fields (e.g., precipitation, clouds, CAPE, CIN, and water vapor) also needs more examination.

Acknowledgements The author thanks Jiao Chen for providing the station CAPE and CIN data used in Fig. 20, and Steve Warren for providing some data used in Hahn et al. (1995).

Author contributions AD did all the work for this study.

Funding This work was funded by University at Albany of SUNY, NSF (Grants AGS-2015780 and OISE-1743738).

Data availability ERA5 data available from https://cds.climate.copernicus.eu/cdsapp#!/dataset/reanalysis-era5-single-levels?tab=form. The averaged 3-hourly data from surface observations are available from https://www2.cgd.ucar.edu/cas/adai/data-dai.html. The CERES data are https://ceres.larc.nasa.gov/data/. The ISCCP data are available from https://www.ncei.noaa.gov/products/climate-data-records/cloud-properties-isccp.

Declarations

Conflict of interest None.

Ethical approval and consent to participate Not applicable.

Consent for publication The author agree to publish the paper in *Climate Dynamics*.

References

Adler RF, Sapiano M, Huffman GJ, Wang J-J, Gu G, Bolvin D, Chiu L, Schneider U, Becker A, Nelkin E, Xie P, Ferraro R, Shin D-B (2018) The Global Precipitation Climatology Project (GPCP) monthly analysis (new version 2.3) and a review of 2017 global precipitation. Atmosphere 9:138. https://doi.org/10.3390/atmos9040138

Bellenger H, Takayabu YN, Ushiyama T, Yoneyama K (2010) Role of diurnal warm layers in the diurnal cycle of convection over the tropical Indian Ocean during MISMO. Mon Weather Rev 138:2426–2433. https://doi.org/10.1175/2010MWR3249.1

Bergman JW, Salby ML (1996) Diurnal variations of cloud cover and their relationship to climatological conditions. J Clim 9:28xx–2820

Cairns B (1995) Diurnal variations of cloud from ISCCP data. Atmos Res 37:133–146

Cao B, Yang X, Li B, Lu Y, Wen J (2022) Diurnal variation in cloud and precipitation characteristics in summer over the Tibetan Plateau and Sichuan Basin. Remote Sens 14:2711. https://doi.org/10.3390/rs14112711

Carbone RE, Tuttle JD (2008) Rainfall occurrence in the U.S. warm season: the diurnal cycle. J Clim 21:4132–4146

Chen D, Dai A (2018) Dependence of estimated precipitation frequency and intensity on data resolution. Clim Dyn 50:3625–3647. https://doi.org/10.1007/s00382-017-3830-7

Chen J, Dai A (2023) The atmosphere has become increasingly unstable during 1979–2020 over the Northern Hemisphere. Geophys Res Lett 50:e2023GL106125. https://doi.org/10.1029/2023GL106125

Chen SS, Houze RA (1997) Diurnal variation and lifecycle of deep convective systems over the tropical Pacific warm pool. Q J R Meteor Soc 123:357–388

Chen G, Iwasaki T, Qin H, Sha W (2014) Evaluation of the warm-season diurnal variability over East Asia in recent reanalyses JRA-55, ERA-Interim, NCEP CFSR, and NASA MERRA. J Clim 27:5517–5537

Chen J, Dai A, Zhang Y, Rasmussen KL (2020) Changes in the convective potential available energy and convective inhibition under global warming. J Clim 33:2025–2050. https://doi.org/10.1175/JCLI-D-19-0461.1

Chen D, Dai A, Hall A (2021) The convective-to-total precipitation ratio and the "drizzling" bias in climate models. J Geophys Res 126:e2020JD034198

Chen G, Wang W-C, Bao Q, Li J (2022) Evaluation of simulated cloud diurnal variation in CMIP6 climate models. J Geophys Res Atmos 127:e2021JD036422. https://doi.org/10.1029/2021JD036422

Chen T, Li J, Zhang Y, Chen H, Li P, Che H (2023a) Evaluation of hourly precipitation characteristics from a global reanalysis and variable-resolution global model over the Tibetan Plateau by using a satellite-gauge merged rainfall product. Remote Sens 15:1013. https://doi.org/10.3390/rs15041013

Chen T, Zhang Y, Li N (2023b) Evaluation of CMIP6 HighResMIP models and ERA5 reanalysis in simulating summer precipitation over the Tibetan Plateau. Atmosphere 14:1015. https://doi.org/10.3390/atmos14061015

Chepfer H, Brogniez H, Noel V (2019) Diurnal variations of cloud and relative humidity profiles across the tropics. Sci Rep 9:16045. https://doi.org/10.1038/s41598-019-52437-6

Clayson CA, Edson JB (2019) Diurnal surface flux variability over western boundary currents. Geophys Res Lett 46:9174–9182. https://doi.org/10.1029/2019GL082826

Covey C, Gleckler PJ, Doutriaux C, Williams DN, Dai A, Fasullo J, Trenberth KE, Berg A (2016) Metrics for the diurnal cycle of precipitation: toward routine benchmarks for climate models. J Clim 29:4461–4471. https://doi.org/10.1175/JCLI-D-15-0664.1

Cui Z, Zhang G, Wang Y, Xie S (2021) Understanding the roles of convective trigger functions in the diurnal cycle of precipitation in the NCAR CAM5. J Clim 34(15):6473–6489. https://doi.org/10.1175/JCLI-D-20-0699.1

Dai A (2001a) Global precipitation and thunderstorm frequencies. Part II: diurnal variations. J Clim 14:1112–1128

Dai A (2001b) Global precipitation and thunderstorm frequencies. Part I: seasonal and interannual variations. J Clim 14:1092–1111

Dai A (2006) Precipitation characteristics in eighteen coupled climate models. J Clim 19:4605–4630

Dai A (2023) The diurnal cycle from observations and ERA5 in surface pressure, temperature, humidity, and winds. Clim Dyn 61:2965–2990. https://doi.org/10.1007/s00382-023-06721-x

Dai A, Deser C (1999) Diurnal and semidiurnal variations in global surface wind and divergence fields. J Geophys Res 104:31109–31125

Dai A, Wang J (1999) Diurnal and semidiurnal tides in global surface pressure fields. J Atmos Sci 56:3874–3891

Dai A, Trenberth KE (2004) The diurnal cycle and its depiction in the Community Climate System Model. J Clim 17:930–951

Dai A, Giorgi F, Trenberth KE (1999) Observed and model simulated diurnal cycles of precipitation over the contiguous United States. J Geophys Res 104:6377–6402

Dai A, Karl TR, Sun B, Trenberth KE (2006) Recent trends in cloudiness over the United States: a tale of monitoring inadequacies. Bull Am Met Soc 87:597–606

Dai A, Xin L, Hsu K-L (2007) The frequency, intensity, and diurnal cycle of precipitation in surface and satellite observations over low- and mid-latitudes. Clim Dyn 29:727–744

Doelling DR, Sun M, Nguyen LT, Nordeen ML, Haney CO, Keyes DF, Mlynczak PE (2016) Advances in geostationary-derived longwave fluxes for the CERES Synoptic (SYN1deg) product. J Atmos Ocean Technol 33:503–521. https://doi.org/10.1175/JTECH-D-15-0147.1

Dommo A, Vondou DA, Philippon N, Eastman R, Moron V, Aloysius N (2022) The ERA5's diurnal cycle of low-level clouds over

Western Central Africa during June–September: dynamic and thermodynamic processes. Atmos Res 280:106426. https://doi.org/10.1016/j.atmosres.2022.106426

Du Y, Rotunno R (2018) Diurnal cycle of rainfall and winds near the south coast of China. J Atmos Sci 75:2065–2082

Flato G, Marotzke J, Abiodun B, Braconnot P, Chou SC, Collins W et al (2013) Evaluation of climate models. In: Stocker TF, Qin D, Plattner G-K, Tignor M, Allen SK, Boschung J et al (eds) Climate change 2013: the physical science basis. Contribution of Working Group I to the Fifth Assessment Report of the Intergovernmental Panel on Climate Change. Cambridge University Press, Cambridge, United Kingdom and New York, NY, USA, pp 741–866

Gray WM, Jacobson RW Jr (1977) Diurnal variation of deep cumulus convection. Mon Weather Rev 105:1171–1188

Gu J, Zhang YH, Yang N, Wang R (2020) Diurnal variability of the planetary boundary layer height estimated from radiosonde data. Earth Planet Phys 4:479–492. https://doi.org/10.26464/epp20200422020

Guo J, Zhang J, Yang K, Liao H, Zhang S, Huang K, Lv Y, Shao J, Yu T, Tong B, Li J, Su T, Yim SHL, Stoffelen A, Zhai P, Xu X (2021) Investigation of near-global daytime boundary layer height using high-resolution radiosondes: first results and comparison with ERA5, MERRA-2, JRA-55, and NCEP-2 reanalysis. Atmos Chem Phys 21:17079–17097. https://doi.org/10.5194/acp-21-17079-2021

Hahn CJ, Warren SG, London J (1995) The effect of moonling on observation of cloud cover at night, and application to cloud climatology. J Clim 8:1429–1446

Hayden LJM, Tan J, Bolvin DT, Huffman GJ (2023) Variations in the diurnal cycle of precipitation and its changes with distance from shore over two contrasting regions as observed by IMERG, ERA5, and Spaceborne Ku radar. J Hydrometeor 24:675–689

Hendon HH, Woodbery K (1993) The diurnal cycle of tropical convection. J Geophys Res 98:16623–16637

Hersbach H, Bell B, Berrisford P, Hirahara S, Horányi A, Muñoz-Sabater J et al (2020) The ERA5 global reanalysis. Q J R Meteorol Soc 146:1999–2049. https://doi.org/10.1002/qj.3803

Huffman G, Bolvin D, Braithwaite D, Hsu K, Joyce R, Xie P (2021) Integrated Multi-satellitE Retrievals for GPM (IMERG), version 06B. NASA's precipitation processing center, https://gpm.nasa.gov/node/3328. Accessed 20 Aug 2021

Jenkins MT, Dai A, Deser C (2023) Seasonal variations and spatial patterns of Arctic cloud changes in association with sea-ice loss during 1950–2019 in ERA5. J Clim 3:735

Kondragunta CR, Gruber A (1996) Seasonal and annual variability of the diurnal cycle of clouds. J Gephys Res 101:21377–21390

Kraus EB (1963) The diurnal precipitation change over the sea. J Atmos Sci 20:551–556

Lee Y-C, Wang Y-C (2021) Evaluating diurnal rainfall signal performance from CMIP5 to CMIP6. J Clim 34:7607–7623. https://doi.org/10.1175/JCLI-D-20-0812.1

Lee M, Schubert SD, Suarez MJ, Held IM, Lau N, Ploshay JJ, Kumar A, Kim H, Schemm JE (2007a) An analysis of the warm-season diurnal cycle over the continental United States and northern Mexico in general circulation models. J Hydrometeorol 8:344–366

Lee M et al (2007b) Sensitivity to horizontal resolution in the AGCM simulations of warm season. J Clim 20:1862–1881. https://doi.org/10.1175/JCLI4090.1

Lee M, Schubert SD, Suarez MJ, Schemm J-KE, Pan H-L, Han J, Yoo S-H (2008) Role of convection triggers in the simulation of the diurnal cycle of precipitation over the United States Great Plains in a general circulation model. J Geophys Res 113:D02111. https://doi.org/10.1029/2007JD008984

Li J, Yu R, Zhou T (2008) Seasonal variation of the diurnal cycle of rainfall in southern contiguous China. J Clim 21:6036–6043. https://doi.org/10.1175/2008JCLI2188.1

Li P, Furtado K, Zhou T, Chen H, Li J, Guo Z, Xiao C (2020) The diurnal cycle of East Asian summer monsoon precipitation simulated by the met office unified model at convection-permitting scales. Clim Dyn 55:131–151

Liang X-Z, Li L, Dai A, Kunkel KE (2004) Regional climate model simulation of summer precipitation diurnal cycle over the United States. Geophys Res Lett 31:L24208. https://doi.org/10.1029/2004GL021054

Lin X, Fowler LD, Randall DA (2000) Diurnal variability of the hydrologic cycle and radiative fluxes: comparisons between observations and a GCM. J Clim 13:4159–4179

Liu S, Liang X-Z (2010) Observed diurnal cycle climatology of planetary boundary layer height. J Clim 23:5790–5809. https://doi.org/10.1175/2010JCLI3552.1

Liu Y, Ackerman SA, Maddux BC, Key JR, Frey RA (2010) Errors in cloud detection over the Arctic using a satellite imager and implications for observing feedback mechanisms. J Clim 23:1894–1907

Liu Z, Gao Y, Zhang G (2022) How well can a convection-permitting-modelling improve the simulation of summer precipitation diurnal cycle over the Tibetan Plateau? Clim Dyn 58:3121–3138. https://doi.org/10.1007/s00382-021-06090-3

Mapes BE, Warner TT, Xu M, Negri AJ (2003) Diurnal patterns of rainfall in northwestern South America. Part I: observations and context. Mon Weather Rev 131:799–812. https://doi.org/10.1175/1520-0493(2003)131%3c0799:DPORIN%3e2.0.CO;2

Mooney PA, Broderick C, Bruyère CL, Mulligan FJ, Prein AF (2017) Clustering of observed diurnal cycles of precipitation over the United States for evaluation of a WRF multiphysics regional climate ensemble. J Clim 30:9267–9286. https://doi.org/10.1175/JCLI-D-16-0851.1

Mori S, Jun-Ichi H, Tauhid YI, Yamanaka MD, Okamoto N, Murata F, Sakurai N, Hashiguchi H, Sribimawati T (2004) Diurnal land-sea rainfall peak migration over Sumatera Island, Indonesian Maritime Continent, Observed by TRMM satellite and intensive rawinsonde soundings. Mon Weather Rev 132:2021–2039. https://doi.org/10.1175/1520-0493(2004)132%3c2021:DLRPMO%3e2.0.CO;2

Nesbitt SW, Zipser EJ (2003) The diurnal cycle of rainfall and convective intensity according to three years of TRMM measurements. J Clim 16:1456–1475. https://doi.org/10.1175/1520-0442(2003)016%3c1456:TDCORA%3e2.0.CO;2

Noel V, Chepfer H, Chiriaco M, Yorks J (2018) The diurnal cycle of cloud profiles over land and ocean between 51° S and 51° N, seen by the CATS spaceborne lidar from the International Space Station. Atmos Chem Phys 18:9457–9473

Ohsawa T, Ueda H, Hayashi T, Watanabe A, Matsumoto J (2001) Diurnal variations of convective activity and rainfall in tropical Asia. J Meteorol Soc Jpn 79:333–352. https://doi.org/10.2151/jmsj.79.333

Oki T, Musiake K (1994) Seasonal change of the diurnal cycle of precipitation over Japan and Malaysia. J Appl Meteor 33:1445–1463

Ploshay JJ, Lau N-C (2010) Simulation of the diurnal cycle in tropical rainfall and circulation during boreal summer with a high-resolution GCM. Mon Weather Rev 138:3434–3453. https://doi.org/10.1175/2010MWR3291.1

Prein AF et al (2015) A review on regional convection-permitting climate modeling: demonstrations, prospects, and challenges. Rev Geophys 53:323–361. https://doi.org/10.1002/2014RG000475

Qin S, Wang K, Wu G, Ma Z (2021) Variability of hourly precipitation during the warm season over eastern China using gauge observations and ERA5. Atmos Res 264:105872

Ramage CS (1952) Diurnal variation of summer rainfall over East China, Korea and Japan. J Atmos Sci 9:83–86. https://doi.org/10.1175/1520-0469(1952)009%3c0083:DVOSRO%3e2.0.CO;2

Randall DA, Dazlich DA (1991) Diurnal variability of the hydrologic cycle in a general circulation model. J Atmos Sci 48:40–62

Ratnam MV, Santhi YD, Rajeevan M, Rao SVB (2013) Diurnal variability of stability indices observed using radiosonde observations over a tropical station: comparison with microwave radiometer measurements. Atmos Res 124:21–33. https://doi.org/10.1016/j.atmosres.2012.12.007

Rossow WB, Schiffer RA (1991) ISCCP cloud data products. Bull Am Meteor Soc 72:2–20

Rozendaal MA, Leovy CB, Klein SA (1995) An observational study of diurnal variations of marine stratiform cloud. J Clim 8:1795–1809

Ruppert JH Jr, Johnson RH (2016) On the cumulus diurnal cycle over the tropical warm pool. J Adv Model Earth Syst 8:669–690

Scaff L, Prein AF, Li Y, Liu C, Rasmussen R, Ikeda K (2020) Simulating the convective precipitation diurnal cycle in North America's current and future climate. Clim Dyn 55:369–382. https://doi.org/10.1007/s00382-019-04754-9

Seidel DJ, Zhang Y, Beljaars A, Golaz J-C, Jacobson AR, Medeiros B (2012) Climatology of the planetary boundary layer over the continental United States and Europe. J Geophys Res 117:D17106. https://doi.org/10.1029/2012JD018143

Serra YL, McPhaden MJ (2004) In situ observations of diurnal variability in rainfall over the tropical Pacific and Atlantic Oceans. J Clim 17:3496–3509. https://doi.org/10.1175/1520-0442(2004)017%3c3496:ISOODV%3e2.0.CO;2

Soden BJ (2000) The diurnal cycle of convection, clouds, and water vapor in the tropical upper troposphere. Geophys Res Lett 27:2173–2176

Song F, Zhang GJ (2017) Improving trigger functions for convective parameterization schemes using GOAmazon observations. J Clim 30(21):8711–8726. https://doi.org/10.1175/JCLI-D-17-0042.1

Song F, Zhang GJ (2018) Understanding and improving the scale dependence of trigger functions for convective parameterization using cloud-resolving model data. J Clim 31:7385–7399. https://doi.org/10.1175/JCLI-D-17-0660.1

Stratton RA, Stirling AJ (2012) Improving the diurnal cycle of convection in GCMs. Q J R Meteorol Soc 138:1121–1134. https://doi.org/10.1002/qj.991

Stubenrauch CJ, Chédin A, Rädel G, Scott NA, Serrar S (2006) Cloud properties and their seasonal and diurnal variability from TOVS Path-B. J Clim 19:5531–5553

Sui C-H, Lau K-M, Takayabu YN, Short DA (1997) Diurnal variations in tropical oceanic cumulus convection during TOGA COARE. J Atmos Sci 54:639–655

Sungmin O, Kirstetter P-E (2018) Evaluation of diurnal variation of GPM IMERG-derived summer precipitation over the contiguous US using MRMS data. Q J R Meteorol Soc 144:270–281. https://doi.org/10.1002/qj.3218

Takayabu YN, Kimoto M (2008) Diurnal march of rainfall simulated in a T106 AGCM and dependence on cumulus schemes. J Meteorol Soc Jpn 86A:163–173

Tan J, Huffman GJ, Bolvin DT, Nelkin EJ (2019) Diurnal cycle of IMERG V06 precipitation. Geophys Res Lett 46:13584–13592. https://doi.org/10.1029/2019GL085395

Tang S, Xie S, Zhang Y, Zhang M, Schumacher C, Upton H, Jensen MP, Johnson KL, Wang M, Ahlgrimm M, Feng Z, Minnis P, Thieman M (2016) Large-scale vertical velocity, diabatic heating and drying profiles associated with seasonal and diurnal variations of convective systems observed in the GoAmazon2014/5 experiment. Atmos Chem Phys 16:14249–14264. https://doi.org/10.5194/acp-16-14249-2016

Tang S, Gleckler P, Xie S, Lee J, Ahn M-S, Covey C, Zhang C (2021) Evaluating diurnal and semi-diurnal cycle of precipitation in CMIP6 models using satellite- and ground-based observations. J Clim 34:3189–3210

Tao C, Xie S, Tang S, Lee J, Ma H-Y, Zhang C, Lin W (2023) Diurnal cycle of precipitation over global monsoon systems in CMIP6 simulations. Clim Dyn 60:3947–3968. https://doi.org/10.1007/s00382-022-06546-0

Tian B, Soden BJ, Wu X (2004) Diurnal cycle of convection, clouds, and water vapor in the tropical upper troposphere: Satellites versus a general circulation model. J Geophys Res 109:D10101. https://doi.org/10.1029/2003JD004117

Wallace JM (1975) Diurnal variations in precipitation and thunderstorm frequency over the conterminous United States. Mon Weather Rev 103:406–419

Wang Y-C, Hsu HH (2019) Improving diurnal rainfall phase over the Southern Great Plains in warm seasons by using a convective triggering design. Int J Climatol 39:5181–5190. https://doi.org/10.1002/joc.6117

Wang B, Kim H-J, Kikuchi K, Kitoh A (2011) Diagnostic metrics for evaluation of annual and diurnal cycles. Clim Dyn 37:941–955. https://doi.org/10.1007/s00382-010-0877-0

Wang Y-C, Pan HL, Hsu HH (2015) Impacts of the triggering function of cumulus parameterization on warm-season diurnal rainfall cycles at the Atmospheric Radiation Measurement Southern Great Plains Site. J Geophys Res 120:10681–10702. https://doi.org/10.1002/2015JD023337

Wang Y-C, Xie S, Tang S, Lin W (2020) Evaluation of an improved convective triggering function: observational evidence and SCM tests. J Geophys Res 125:e2019JD031651. https://doi.org/10.1029/2019JD031651

Wei Y, Pu Z (2022) Diurnal cycle of precipitation and near-surface atmospheric conditions over the maritime continent: land–sea contrast and impacts of ambient winds in cloud-permitting simulations. Clim Dyn 58:2421–2449. https://doi.org/10.1007/s00382-021-06012-3

Wu Y, Huang A, Huang D, Chen F, Yang B, Zhou Y, Fang D, Zhang L, Wen L (2018) Diurnal variations of summer precipitation over the regions east to Tibetan Plateau. Clim Dyn 51:4287–4307. https://doi.org/10.1007/s00382-017-4042-x

Wylie DP, Woolf HM (2002) The diurnal cycle of upper tropospheric clouds measured by GOES-VAS and the ISCCP. Mon Weather Rev 130:171–179

Xie S, Wang Y-C, Lin W, Ma H-Y, Tang Q, Tang S et al (2019) Improved diurnal cycle of precipitation in E3SM with a revised convective triggering function. J Adv Model Earth Syst 11:2290–2310. https://doi.org/10.1029/2019MS001702

Yan Y, Zhang L, Song X, Wang G, Chen C (2021) Diurnal variation in surface latent heat flux and the effect of diurnal variability on the climatological latent heat flux over the tropical oceans. J Phys Oceanogr 51:3401–3415. https://doi.org/10.1175/JPO-D-21-0128.1

Yang G-Y, Slingo J (2001) The diurnal cycle in the tropics. Mon Weather Rev 129:784–801

Yang S, Smith EA (2006) Mechanisms for diurnal variability of global tropical rainfall observed from TRMM. J Clim 19:5190–5226. https://doi.org/10.1175/JCLI3883.1

Yeo H et al (2022) Arctic cloud properties and associated radiative effects in the three newer reanalysis datasets (ERA5, MERRA-2, JRA-55): discrepancies and possible causes. Atmos Res 270:106080. https://doi.org/10.1016/j.atmosres.2022.106080

Yokoi S, Mori S, Katsumata M, Geng B, Yasunaga K, Syamsudin F, Nurhayati, Yoneyama K (2017) Diurnal cycle of precipitation observed in the western coastal area of Sumatra Island: offshore preconditioning by gravity waves. Mon Weather Rev 145:3745–3761. https://doi.org/10.1175/MWR-D-16-0468.1

Young AH, Knapp KR, Inamdar A, Hankins W, Rossow WB (2018) The International Satellite Cloud Climatology Project H-Series climate data record product. Earth Syst Sci Data 10:583–593. https://doi.org/10.5194/essd-10-583-2018

Yu R, Li J (2016) Regional characteristics of diurnal peak phases of precipitation over contiguous China. Acta Meteorol Sin 74:18–30. https://doi.org/10.11676/qxxb2016.011. (**in Chinese with English abstract**)

Yu R, Zhou T, Xiong A, Zhu Y, Li J (2007) Diurnal variations of summer precipitation over contiguous China. Geophys Res Lett 34:L01704. https://doi.org/10.1029/2006GL028129

Yu R, Li J, Chen H, Yuan W (2014) Progress in studies of the precipitation diurnal variation over contiguous China. J Meteorol Res 28:877–902. https://doi.org/10.1007/s13351-014-3272-7

Yuan W, Yu R, Chen H, Li J, Zhang M (2010) Subseasonal characteristics of diurnal variation in summer monsoon rainfall over central eastern China. J Clim 23:6684–6695

Yuan W, Yu R, Zhang M, Lin W, Chen H, Li J (2012) Regimes of diurnal variation of summer rainfall over subtropical East Asia. J Clim 25:3307–3320. https://doi.org/10.1175/JCLI-D-11-00288.1

Zelinka MD, Myers TA, McCoy DT, Po-Chedley S, Caldwell PM, Ceppi P, Klein SA, Taylor KE (2020) Causes of higher climate sensitivity in CMIP6 models. Geophys Res Lett 47:e2019GL085782. https://doi.org/10.1029/2019GL085782

Zhang Y, Klein SA (2010) Mechanisms affecting the transition from shallow to deep convection over land: inferences from observations of the diurnal cycle collected at the ARM southern Great Plains site. J Atmos Sci 67:2943–2959. https://doi.org/10.1175/2010JAS3366.1

Zhang Y, Sun K, Gao Z, Pan Z, Shook MA, Li D (2020) Diurnal climatology of planetary boundary layer height over the contiguous United States derived from AMDAR and reanalysis data. J Geophys Res 125:e2020JD032803. https://doi.org/10.1029/2020JD032803

Zhao D, Dong W, Lin Y, Hu Y, Cao D (2022) Diurnal variation of precipitation over the high mountain Asia: spatial distribution and its seasonality. J Hydrometeor 23:1945–1959. https://doi.org/10.1175/JHM-D-21-0243.1

Zhao Y, Li J, Li P (2023a) Diurnal cycle of precipitation over the southeastern Tibetan Plateau and surrounding regions: insights from intensity–frequency structure. Int J Climatol 43:3284–3297. https://doi.org/10.1002/joc.8029

Zhao Y, Li J, Zhang L, Deng C, Li Y, Jian B, Huang J (2023b) Diurnal cycles of cloud cover and its vertical distribution over the Tibetan Plateau revealed by satellite observations, reanalysis datasets, and CMIP6 outputs. Atmos Chem Phys 23:743–769. https://doi.org/10.5194/acp-23-743-2023

Zheng YG, Gong YD, Chen J, Ian FY (2019) Warm-season diurnal variations of total, stratiform, convective, and extreme hourly precipitation over central and eastern China. Adv Atmos Sci 36(2):143–159. https://doi.org/10.1007/s00376-018-7307-3

Zhou T, Yu R, Chen H, Dai A, Pan Y (2008) Summer precipitation frequency, intensity, and diurnal cycle over China : a comparison of satellite data with raingauge observations. J Clim 21:3997–4010

Zhu Z, Wang M, Wang J, Ma X, Luo J, Yao X (2023) Diurnal variation characteristics of the surface sensible heat flux over the Tibetan Plateau. Atmosphere 14:128. https://doi.org/10.3390/atmos14010128